Dendritic domain-specific sampling of long-range axons shapes feedforward and feedback connectivity of L5 neurons

Alessandro R. Galloni[1,2], Zhiwen Ye[1] and Ede Rancz[1*]

[1]The Francis Crick Institute, London, United Kingdom; [2]University College London, United Kingdom.

*For correspondence: ede.rancz@crick.ac.uk

Abstract

Feedforward and feedback pathways interact in specific dendritic domains to enable cognitive functions such as predictive inference and learning. Based on axonal projections, hierarchically lower areas are thought to form synapses primarily on dendrites in middle cortical layers, while higher-order areas are posited to target dendrites in layer 1 and in deep layers. However, the extent to which functional synapses form in regions of axo-dendritic overlap has not been extensively studied. Here, we use viral tracing in the visual cortex of mice to map brain-wide inputs to a genetically-defined population of layer 5 pyramidal neurons. Furthermore, we provide a comprehensive map of input locations through subcellular optogenetic circuit mapping. We show that input pathways target distinct dendritic domains with far greater specificity than appears from their axonal branching, often deviating substantially from the canonical patterns. Common assumptions regarding the dendrite-level interaction of feedforward and feedback inputs may thus need revisiting.

Introduction

One of the key organizing principles of connectivity within the neocortex is thought to be hierarchy between cortical areas. This notion was originally proposed by Hubel & Wiesel (Hubel & Wiesel 1962) to account for the increasing receptive field complexity in areas progressively further from the retina. In purely feedforward (FF) networks, such as artificial neural nets used successfully in computer vision (LeCun et al 2015), hierarchy is generally defined by synaptic distance from the sensory periphery. However, in highly recurrent networks like the cortex, it is not possible to apply this definition consistently beyond the initial levels. Instead, the laminar patterns of axonal projections are often used to deduce relative levels of hierarchy. For example, the projection from primary to secondary visual cortex, which is classically defined as FF, is characterised by dense axon terminations in middle cortical layers (particularly L4). Meanwhile, the projection from secondary to primary visual cortex, feedback (FB) by definition, primarily targets L1, and to a lesser extent deeper layers (Rockland & Pandya 1979). This pattern of FF and FB projections also appears in many other brain regions, and has been used as a proxy to describe the hierarchical relationships between a large number of areas across the brain (D'Souza et al 2016, D'Souza et al 2020, Felleman & Van Essen 1991, Harris et al 2019, Wang et al 2020b, Zeng 2018).

Projections, however, do not guarantee functional connections. The link between the two is called Peters' rule, which postulates that the probability of synaptic connections can be predicted from the overlap between axonal and dendritic arbours (Rees et al 2017). While synapses can only form where there is overlap between axons and dendrites, the converse is not necessarily true. The link between axo-dendritic overlap and connection probability may thus be overly simplistic and requires further scrutiny. While some studies have found support for Peters' rule at the level of functional synaptic connectivity for interneurons (Fino & Yuste 2011, Packer et al 2013, Rieubland et al 2014), its general applicability has been refuted, at least for local networks, by dense anatomical reconstructions of retinal (Briggman et al 2011, Helmstaedter et al 2013, Kim et al 2014, Krishnaswamy et al 2015) and cortical circuits (Kasthuri et al 2015, Lee et al 2016). To investigate how this principle applies to long-range projections, a technique that has become widely adopted is subcellular channelrhodopsin-assisted circuit mapping (sCRACM). Here optogenetics is combined with spatially targeted optical stimulation to map the distribution of synaptic currents for a given input (Petreanu et al 2009). While this has been used to show that different presynaptic populations target dendritic subdomains with high specificity (Collins et al 2018, Hooks et al 2013, Little & Carter 2012, Yamawaki et al 2019), the extent to which this can be explained and predicted by the distribution of axons and dendrites remains largely an open question. This is particularly relevant for the case of layer 5 pyramidal neurons (L5PN), given their central role in several theories of cortical computation (Aru et al 2020, Guerguiev et al 2017, Larkum 2013, Richards et al 2019). Furthermore, the interaction between FF and FB information streams across cortical layers (Larkum et al 2018) is thought to underlie the brain's ability to modulate sensory perception (Larkum 2013, Takahashi et al 2020, Takahashi et al 2016) and implement global inference algorithms such as predictive coding (Shipp 2016).

All these approaches assume Peters' rule, according to which FF connectivity to L5PNs should target primarily basal dendrites, while FB connectivity preferentially synapses on the apical tuft. The evidence for this remains circumstantial and a direct examination of Peters' rule across a large number of inputs to individual L5PNs remains to be done.

Here we present a comprehensive description of the functional input connectivity to a population of thick-tufted layer 5 (ttL5) pyramidal neurons in the visual cortex. In particular, we set out to do three things: determine the source of input connectivity to ttL5 neurons using monosynaptically restricted rabies tracing (Kim et al 2015, Reardon et al 2016), create a census of subcellular input maps using sCRACM, and test Peters' rule directly by comparing synaptic input maps to the respective axonal projection maps. As higher order cortical regions are likely to receive a broader diversity of long-range inputs, we recorded from a genetically defined population (Colgalt2-Cre; Groh et al 2010, Kim et al 2015) with sparse and ttL5-specific labelling spanning the mouse medial secondary visual areas (VISam, VISpm and RSPagl, collectively referred to as V2m following Franklin & Paxinos 2007).

Results

Brain-wide input map to V2m ttL5 pyramidal neurons

We employed a monosynaptically restricted rabies virus approach (Reardon et al 2016, Wickersham et al 2007) to generate a presynaptic input map of V2m ttL5 neurons. Briefly, a mix of adeno-associated viruses carrying floxed N2c G-protein, or TVA-receptor and EGFP genes were injected into V2m of Colgalt2-Cre mice under stereotaxic guidance. Five to seven days later, mCherry expressing EnvA-CVS-N2c-ΔG rabies virus was injected at the same location. After a further 10-12 days, the brains (n = 3) were fixed and imaged using serial section 2-photon tomography. These were then registered to the Allen common coordinate framework (CCFv3) and presynaptic cell bodies were detected and counted using an automated pipeline (see Methods for details). Names and abbreviation for brain areas follow the Allen CCFv3 (Wang et al 2020a) and are given in Figure 1—figure supplement 1.

Cell density maps for an example experiment are shown in Figure 1. The fifteen starter cells scattered across V2m (Figure 1A) revealed presynaptic input neurons in a broad range of cortical and subcortical areas, with the vast majority located in the ipsilateral cortex and thalamus (94 ± 1%; n = 3 mice; Figure 1B,C). We have grouped the most prominent input areas into proximal cortex (53%), distal cortex (8%) and thalamus (19%; Figure 1E) and calculated total input proportion as the number of presynaptic cells in an input area divided by the total number of presynaptic cells (Figure 1—supplementary table 1).

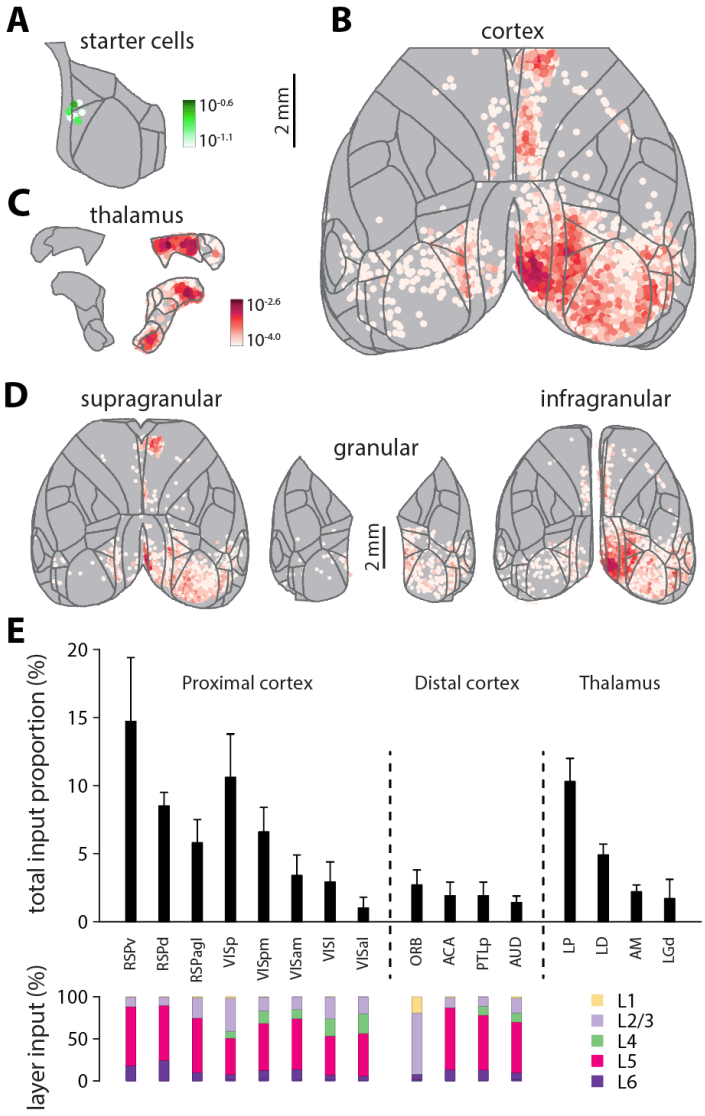

Figure 1. Whole-brain input map to V2m ttL5 neurons. A. Starter cell density map from an example experiment. **B.** Cortical input cell density map projected onto the horizontal plane. **C.** Thalamic input cell density map projected onto two coronal planes. **D.** Input cell density maps across supragranular, granular and infragranular layers. Density scales (in units of μm^{-2}) were calculated using a 90 x 90 µm grid then normalized to the total number of starter or presynaptic cells and are the same for B-D; area names can be found in Figure 1—figure supplement 1. **E.** Total input proportion map for selected input areas. Bottom: distribution of input cells across cortical layers. Average of 3 experiments.

The majority of input was provided by VISp (10.6 ± 3.2 %) and the three RSP areas (29 % in total), while orbitofrontal cortex (ORB; 2.7 ± 1.1 %) and the anterior cingulate area (ACA; 1.9 ± 1 %) provided the most significant (albeit still modest) distal cortical input. Interestingly, while the majority of cortical input cells were located in the infragranular layers, especially layer 5, input from ORB was almost exclusively from layer 2/3 (Figure 1D,E). Prominent thalamic inputs were also observed, originating mainly in the

lateral posterior nucleus (LP, 10.3 ± 1.7 %) and anterior thalamic nuclei (ATN, composed of areas LD, 4.9 ± 0.8 %, and AM, 2.2 ± 0.5 %). Cell counts for individual experiments and all brain areas can be found in Figure 1—supplementary table 1.

To understand the organization of inputs onto ttL5 neurons in V2m, we chose to focus our efforts on 7 prominent input areas. VISp and V2m for FF input; RSPg (RSPv, RSPd), ACA and ORB for cortical FB input; and LP and ATN for thalamic FB connections. These areas in total represent 72% of all presynaptic input neurons.

Axonal projection patterns in V2m define putative synaptic regions

To determine axonal projection patterns of the previously selected areas and subcellular synaptic connectivity to ttL5 neurons in V2m, we injected AAVs expressing Chronos-eGFP into input areas. Acute brain slices were prepared after a minimum of 3 weeks of survival to obtain electrophysiological recordings. The brain slices were then fixed, and axonal projections imaged using confocal microscopy.

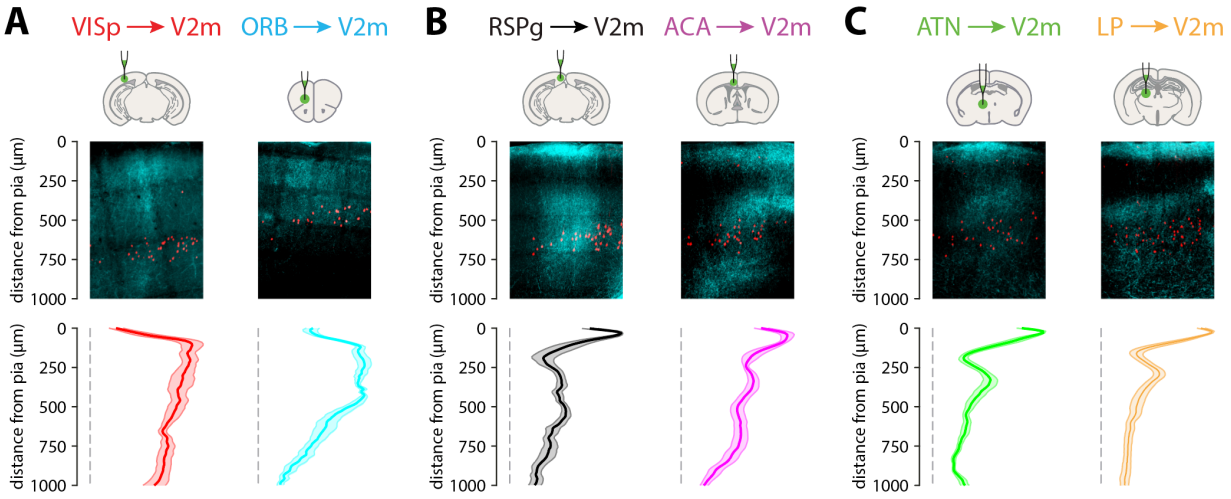

Figure 2. Axonal projection densities from different input areas. A-C. Top: coronal brain pictograms indicating the injection sites. Middle: example confocal images from V2m showing axonal projections (cyan) and Colgalt2-Cre cell bodies (red). Bottom: projection density profiles averaged across 3-5 injections.

The spatial distribution of axons followed three basic patterns. Axons from VISp and ORB were densest in layer (L) 2/3 and L5 while little projection was apparent in L1, reminiscent of the classical FF projection pattern (Figure 2A). In contrast, axons from RSPg and ACA showed an FB-like pattern with dense labelling in the middle part of L1 followed by sparse labelling in L2 and diffuse axons in layers 3, 5 and 6 (Figure 2B). The final group, which consists of the thalamic projections from LP and ATN, showed the classical FB pattern strongly innervating the external part of L1, with a secondary peak in L3, but little or no projections in layers 2, 5 and 6 (Figure 2C).

Having established where it is possible for synaptic connections to form, we next sought to determine the dendritic location of synaptic inputs from the selected areas.

Subcellular optogenetic input mapping reveals diverse targeting of dendritic domains by input areas

To determine the spatial distribution of synaptic inputs to ttL5 neurons in V2m, we performed sCRACM experiments from selected input areas identified by rabies tracing. Following expression of the optogenetic activator Chronos, we made voltage-clamp recordings (at -70 mV) from ttL5 (Colgalt2-Cre) neurons in acute brain slices. Optical stimulation with a 463 nm laser was spatially targeted using a digital micromirror device (Figure 3A). Sodium and potassium channels were blocked using TTX (1µm) and 4-AP (100 µm) to ensure that evoked currents were restricted to directly stimulated nerve terminals and to enhance presynaptic release, respectively. The stimulus consisted of 24 x 12 spots of light in a 1000 x 500 µm grid aligned to the axis of the apical dendrite of the recorded neuron and covering the whole depth of cortex. For each input area, we recorded 14-27 cells from 3-9 animals.

To estimate synaptic strength at each location, we measured the area of evoked synaptic currents (corresponding to charge; Figure 3B) and made normalized 2D maps of the spatial distribution of inputs (Figure 3C). Individual maps were then aligned (either to the pia or soma) and averaged. To quantify the spatial location of inputs, we projected the average 2D maps in directions parallel (Figure 3C) or perpendicular to the apical dendrite (Figure 3D). Furthermore, we defined the spatial distribution of the three main dendritic compartments - the apical tuft, oblique, and basal dendrites - on the basis of 11 morphologically reconstructed Colgalt2-Cre neurons. The horizontal projection of the average morphology was used to separate the contribution of each dendritic domain to the total synaptic input (Figure 3D; see Methods for details).

To test the detectability of distal inputs regardless of their synaptic strength, we examined the correlation between the location of synaptic input and the total synaptic charge evoked by full-field stimulation (Figure 3—figure supplement 1). No correlation was found for any of the recorded areas, suggesting no detection bias for distal inputs.

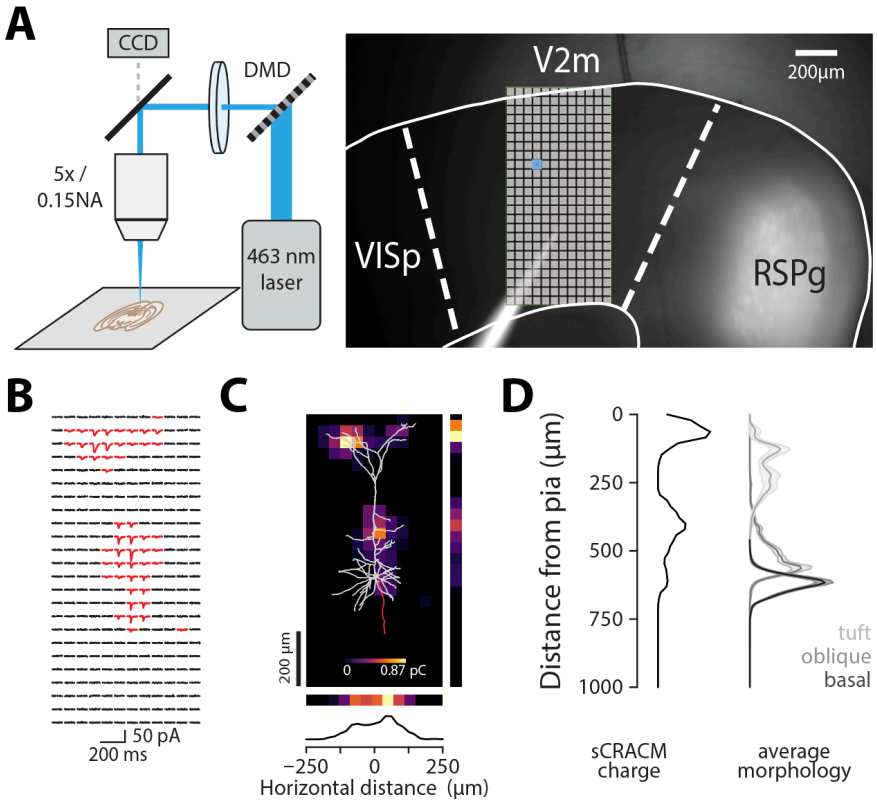

Figure 3. Using sCRACM to map subcellular connectivity from proximal cortical input areas. A. Experimental setup and micrograph showing a brain slice with Chronos expression in RSPg and recording pipette in V2m. The stimulation grid is overlaid, and an example spot is highlighted in blue. **B**. example sCRACM recording of excitatory synaptic currents (red > 7 x S.D.) for an example neuron. **C.** Charge heatmap corresponding to recording in B with the morphology of the recorded neuron overlaid. **D.** Normalized vertical profile of input map in C. Right: average morphology profile used for dendritic domain deconvolution.

Primary visual cortex

We first recorded optically evoked synaptic responses arising from VISp axons (n = 14 cells from 7 animals, average soma depth 493 ± 18 µm; Figure 4A). The apical tuft received 57% of the input, with a peak input located 198 µm from the pia (Figure 4—supplementary table 1). The remaining input was spread between the oblique compartment, receiving 25%, and basal dendrites, receiving 18% of the total input. The majority of recorded neurons had the peak input in the apical compartment (n = 10 / 14) while a few cells lacked apical input (Figure 4—figure supplement 1A). Soma depth for individual recordings did not correlate with either tuft or perisomatic input location, suggesting that VISp synapses on ttL5 neurons target cortical layers rather than specific dendritic domains (Figure 4—figure supplement 1A). The horizontal input distribution showed a slight medial skew (towards RSPg), most prominent in the oblique and basal compartments (-42 µm for both; -21 µm in the tuft; Figure 4—figure supplement 1B). The total synaptic charge measured via the somatic recording following full-field stimulation was 1.46 ± 0.33 pC

169 (Figure 4A). VISp thus provides moderate direct input to ttL5 neurons in V2m, primarily targeting the
170 proximal part of the apical tuft (0.84 pC) with smaller input arriving to the oblique (0.36 pC) and basal
171 (0.26 pC) compartments.

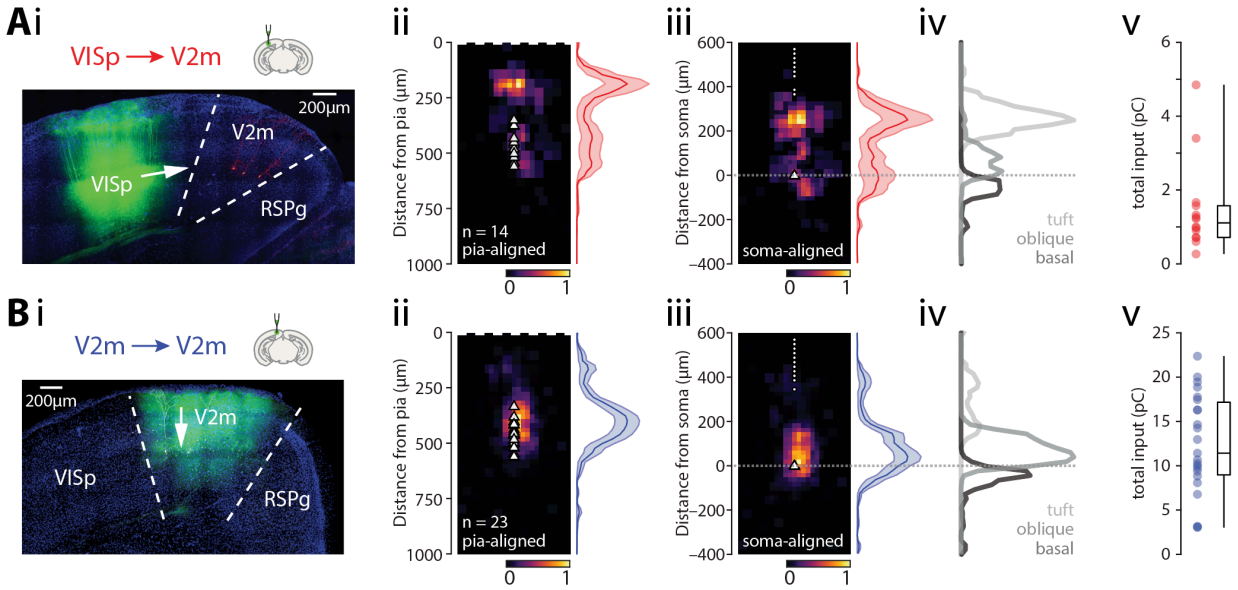

172

173 **Figure 4. Subcellular connectivity maps of FF input areas. A.** *i*: confocal image of a representative brain slice
174 (blue = DAPI) showing the injection site in VISp (green) and recorded neurons in V2m (red). *ii*: pia-aligned average
175 sCRACM heatmap for VISp inputs. Triangles represent soma locations. The vertical profile indicates the normalized
176 average and SEM of the input distributions across all recorded neurons. *iii*: Same as in ii but aligned on the soma
177 location. Dots indicate pia locations. *iv*: Normalized input magnitude deconvolved with the average morphology.
178 Dotted line indicates soma location. *v*: Box plot showing total input charge recorded during full-field stimulation. **B.**
179 Same as in A but for Cre-off Chronos injections into V2m.

180 *Local input from V2m*

181 To estimate the distribution of local input we used a Cre-off viral strategy, limiting Chronos expression to
182 non-Colgalt2-Cre neurons (n = 23 cells from 4 animals, average soma depth 482 ± 12 µm; Figure 4B).
183 When testing this strategy using the much denser Rbp4-Cre line, we found that only a very small
184 proportion of Cre-positive cells expressed Chronos (3%, Figure 4—figure supplement 2). The peak input
185 was located close to the soma, at 427 µm from the pia. The oblique compartment received the majority
186 (62%) of this input, with the basal dendrites and apical tuft receiving 23% and 16%, respectively, of the
187 total input (Figure 4—supplementary table 1). For the majority of recorded neurons, the peak input
188 occurred perisomatically (n = 22 / 23; Figure 4—figure supplement 3A). There was significant correlation
189 between soma depth and perisomatic input location, suggesting compartment-specific targeting of
190 individual ttL5 neurons rather than generic targeting of the cortical layer (Figure 4—figure supplement
191 3A). The horizontal input distribution showed a very slight lateral bias (-21 µm for all peaks; Figure 4—

192 figure supplement 3B). The total synaptic charge triggered by full-field stimulation was 12.61 ± 1.17 pC
193 (Figure 4B). Local neurons thus provide large direct input to ttL5 neurons in V2m, primarily targeting the
194 oblique (7.78 pC) compartment, with smaller input arriving to the basal (2.85 pC) and tuft (1.98 pC)
195 compartments.

196 *Granular retrosplenial area*

197 Next, we recorded optically evoked synaptic responses arising from RSPg axons (n = 26 cells from 9
198 animals, average soma depth 491 ± 13 µm; Figure 5A). The overall input displayed a bimodal distribution
199 peaking at 135 and 510 µm from the pia. The apical tuft received 25% of the input, with the oblique
200 compartment receiving 42% and basal dendrites 32% of the total input (Figure 4—supplementary table
201 1). For the majority of recorded neurons, the peak input targeted the perisomatic dendrites (n = 24 / 26;
202 Figure 5—figure supplement 1A). While there was no correlation between soma depth and tuft input, the
203 perisomatic input location followed the soma location to a significant level, suggesting that RSPg axons
204 target ttL5 dendrites at a single-cell level with specificity going beyond the general cortical layer (Figure
205 5—figure supplement 1A). The horizontal input distribution showed no lateral bias (Figure 5—figure
206 supplement 1B). Total synaptic charge triggered by full-field stimulation was 3.56 ± 0.58 pC (Figure 5A).
207 RSPg thus provides a relatively moderate direct input to ttL5 neurons in V2m, primarily targeting the
208 oblique (1.5 pC) and basal (1.15 pC) compartments with smaller input arriving to the more distal part of
209 the apical tuft (0.9 pC).

210 *Anterior cingulate area*

211 Next, we recorded optically evoked synaptic responses arising from ACA axons (n = 27 cells from 5
212 animals, average soma depth 461 ± 8 µm; Figure 5B). The overall input was bimodal, peaking at 94 µm
213 and 448 µm from the pia. The apical tuft received 27% of the input, with the oblique compartment
214 receiving 43% and basal dendrites 30% of the total input (Figure 4—supplementary table 1). The majority
215 of recorded neurons had the peak input located perisomatically (n = 25 / 27; Figure 5-figure supplement
216 1A). There was no correlation between soma depth and tuft input, while the perisomatic input location
217 followed the soma to a significant degree, suggesting single-cell sublayer specificity of ACA axons (Figure
218 5—figure supplement 2A). The horizontal input distribution showed a slight lateral bias (tuft 21 µm,
219 oblique -21 µm; Figure 5—figure supplement 2B). The total synaptic charge triggered by full-field
220 stimulation was 8.75 ± 1.18 pC (Figure 5B). ACA thus provides a large direct input to ttL5 neurons in
221 V2m, primarily targeting the oblique (3.77 pC) compartment with smaller input arriving to the basal (2.64
222 pC) and most distal part of the apical tuft (2.34 pC).

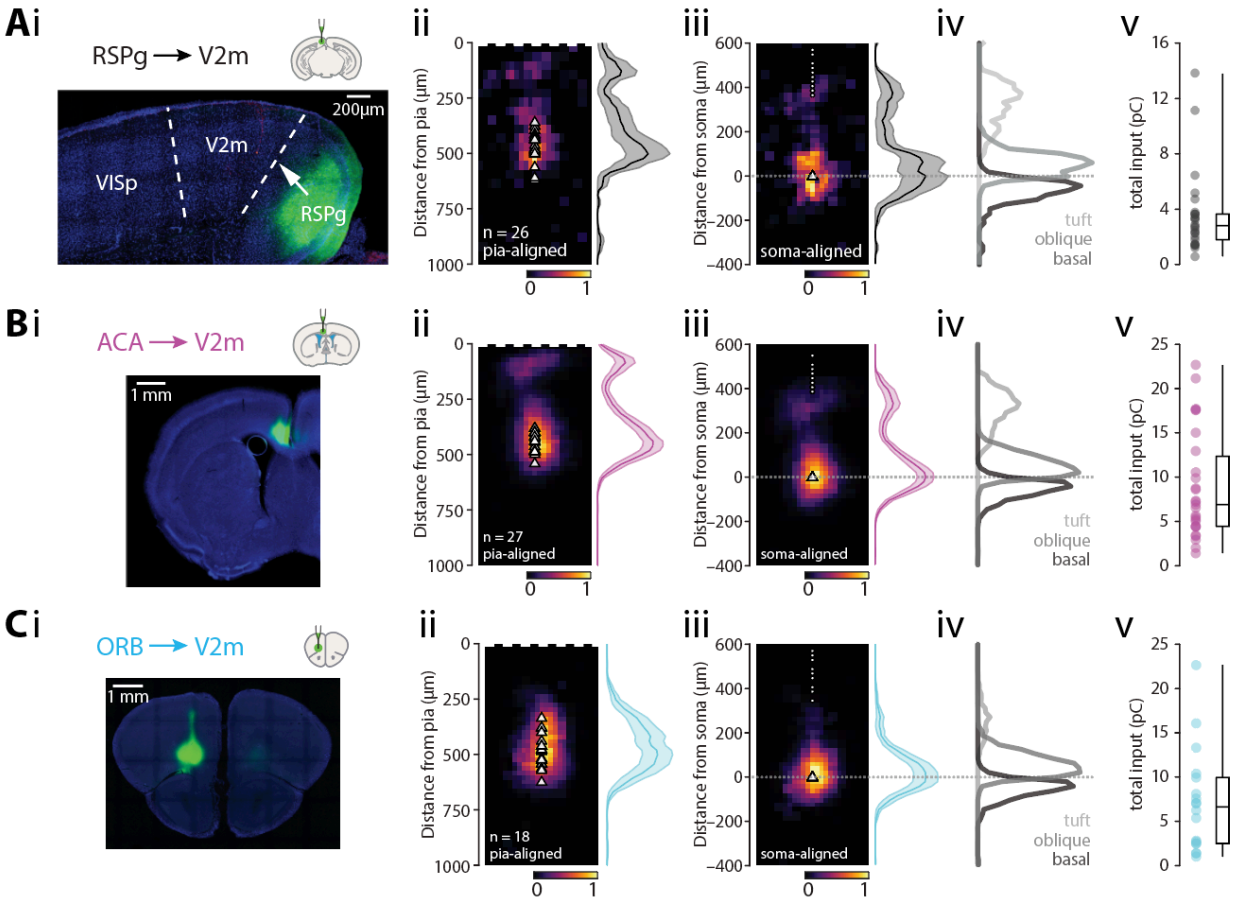

Figure 5. Subcellular connectivity maps of cortical FB areas. A. *i:* confocal image of a representative brain slice (blue = DAPI) showing the injection site in RSPg (green). *ii:* pia-aligned average sCRACM heatmap for RSPg inputs. Triangles represent soma locations. The vertical profile indicates the normalized average and SEM of the input distributions across all recorded neurons. *iii:* Same as in *ii* but aligned on the soma location. Dots indicate pia locations. *iv:* Normalized input magnitude deconvolved with the average morphology. Dotted line indicates soma location. *v:* Box plot showing total input charge recorded during full-field stimulation. **B.** Same as in A but for Chronos injections into ACA. **C.** Same as in A but for Chronos injections into ORB.

Orbitofrontal cortex

Optically evoked synaptic responses arising from ORB axons (n = 18 cells from 3 animals, average soma depth 502 ± 18 µm; Figure 5C) showed a strong perisomatic bias, with a peak at 510 µm from the pia. The apical tuft received only 8% of all input, with the oblique compartment receiving 55% and basal dendrites 37% of the total input (Figure 4—supplementary table 1). This distribution was also highly homogeneous across neurons, with almost all recorded neurons having their peak input in the perisomatic region (n = 17/18; Figure 5—figure supplement 3A). Interestingly, the input location of individual cells followed their soma depth significantly, suggesting ORB axons are targeting specific dendrites of individual ttL5 neurons rather than the cortical layer in general (Figure 5—figure supplement

3A). The horizontal input distribution showed no lateral bias (Figure 5—figure supplement 3B). The total synaptic charge triggered by full-field stimulation was 7.11 ± 1.36 pC (Figure 5C). ORB thus provides a large direct input to ttL5 neurons in V2m, primarily targeting the oblique (3.94 pC) and basal (2.63 pC) compartments, with slight input arriving to the proximal part of the apical tuft (0.55 pC).

Anterior thalamic nuclei

Finally, we recorded optically evoked synaptic responses from thalamic axons, starting with the ATN (n = 16 cells from 5 animals, average soma depth 458 ± 11 µm; Figure 6A). This input had peaks at both 115 µm and 385 µm from the pia, with the apical tuft receiving the majority (68%) of the input, while the oblique compartment received 25% and basal dendrites a mere 7% of the total input (Figure 4—supplementary table 1). The majority of recorded neurons had the peak input in the tuft compartment (n = 9 / 16) and while all cells had some tuft input, in 7/16 cells the input peak was located perisomatically (Figure 6—figure supplement 1A). There was no correlation between soma depth and either tuft or perisomatic input location for individual recordings, suggesting ATN axons are targeting cortical layers rather than specific ttL5 dendrites directly (Figure 6—figure supplement 1A). The horizontal input distribution showed a slight lateral bias (21 µm for tuft and -21 µm for obliques and basal peaks; Figure 6—figure supplement 1B). The total synaptic charge triggered by full-field stimulation was 2.55 ± 0.3 pC (Figure 6A). ATN thus provides a moderate direct input to ttL5 neurons in V2m, primarily targeting the more distal part of the apical tuft (1.73 pC) while the oblique (0.65 pC) and the basal (0.17 pC) compartment received less input.

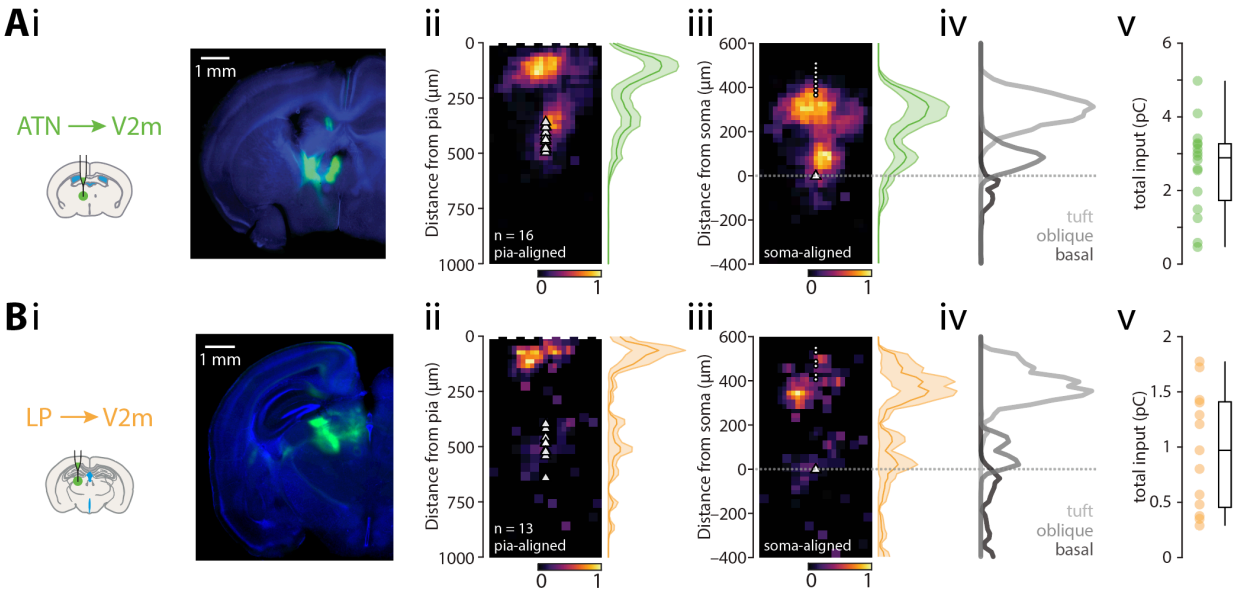

Figure 6. Subcellular connectivity maps of thalamic input areas. A. *i:* confocal image of a representative brain slice (blue = DAPI) showing the injection site in ATN (green). *ii:* pia-aligned average sCRACM heatmap for ATN inputs. Triangles represent soma locations. The vertical profile indicates the normalized average and SEM of the input distributions across all recorded neurons. *iii:* Same as in *ii* but aligned on the soma location. Dots indicate pia

264 locations. *iv:* Normalized input magnitude deconvolved with the average morphology. Dotted line indicates soma
265 location. *v:* Box plot showing total input charge recorded during full-field stimulation. **B.** Same as in A but for Chronos
266 injections in LP.

267 *Lateral posterior nucleus of the thalamus*

268 Lastly, we recorded optically evoked synaptic responses arising from LP axons (n = 13 cells from 5
269 animals, average soma depth 502 ± 19 µm; Figure 6B). Due to excessive retrograde labelling resulting in
270 direct photocurrent in the recorded V2m cells, a 1:10 dilution of virus was used for these injections. The
271 absolute value of the evoked input is thus likely an underestimate. As with ATN axons, the LP input was
272 strongly biased towards the most superficial part of the cortex and peaked at 73 µm from the pia. The
273 apical tuft received the vast majority (68%) of the input, with the oblique compartment receiving 18% and
274 basal dendrites 13 % of the total input (Figure 4—supplementary table 1). The majority of recorded
275 neurons had the peak input in the tuft compartment (n = 11/13; Figure 6—figure supplement 2A). There
276 was no correlation between soma depth and either tuft or perisomatic input location for individual
277 recordings, suggesting LP axons are targeting cortical layers rather than specific ttL5 dendrites directly
278 (Figure 6—figure supplement 2A). The horizontal input distribution showed strong lateral bias (-83 µm for
279 tuft and 63 µm for the oblique peak; Figure 6—figure supplement 2B). The total synaptic charge triggered
280 by full-field stimulation was 0.97 ± 0.15 pC (Figure 6B). LP thus provides small direct input to ttL5 neurons
281 in V2m, primarily targeting the most distal part of the apical tuft (0.67 pC) compartment with smaller input
282 arriving to the oblique (0.18 pC) and the basal (0.13 pC) compartments.

283 Comparison of anatomical and functional connectivity maps

284 To accurately estimate morphological overlap between axons and dendrites, we convolved the axonal
285 projection maps with the average dendritic morphology, resulting in the predicted input distribution one
286 would expect to see based on Peters' rule. When overlaying this with the pia-aligned vertical sCRACM
287 maps, the alignments between functional synapses and the axo-dendritic maps were diverse (Figure 7A).
288 For some regions, like ORB perisomatic and LP tuft inputs, a clear correspondence could be seen
289 between predicted and measured input distributions. A lesser degree of overlap can also be seen in the
290 VISp perisomatic or ACA tuft inputs. For other inputs, however, strong functional input could be detected
291 where there is very little overlap between dendrites and axons, such as at VISp tuft inputs. This stood in
292 stark contrast to the ORB projection, for which the opposite was true, and apical regions of dense
293 morphological overlap of axons and dendrites resulted in no functional input.

294 Next we examined the correspondence between the anatomical input connectivity results obtained from
295 rabies tracing and the functional connectivity results obtained by sCRACM. The proportion of rabies-
296 labelled inputs (only taking into account the 7 areas investigated by sCRACM) showed a strong
297 contribution from RSPg and modest input cell proportions for the more distal cortical regions (e.g. ACA,

ORB). The proportional sCRACM input calculated from the full-field stimuli however shows an altogether different and effectively anti-correlated picture (Figure 7B), with modest input from RSPg and most input arriving from V2m, ACA and ORB.

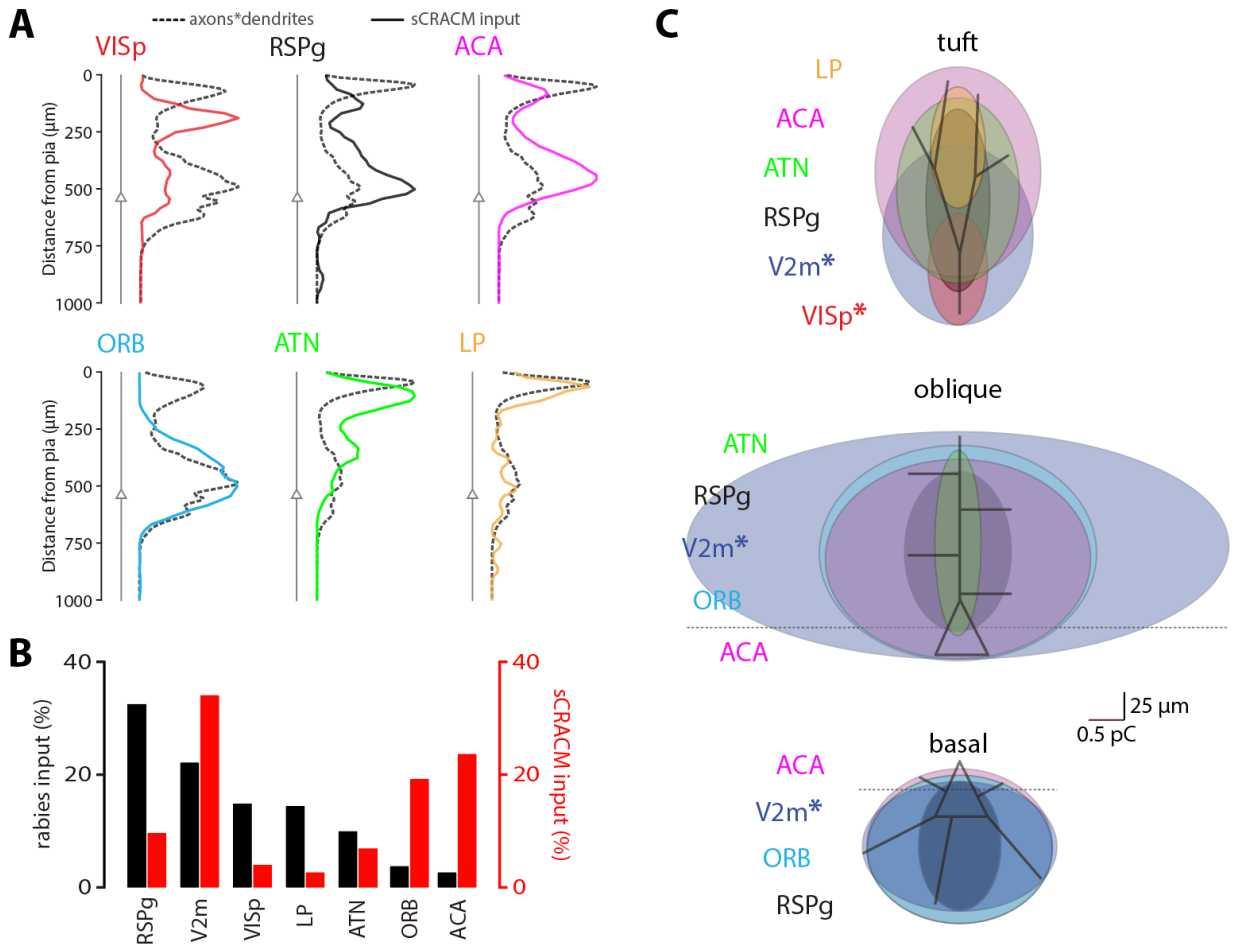

Figure 7. Comparing different input maps. A. Axonal density distribution convolved with dendritic morphology (dotted black lines) overlaid with pia-aligned synaptic input distribution (coloured lines). Six input areas are shown. Triangles represent soma location in average morphology. **B.** Proportion of input cells across 7 areas established by rabies tracing (black) and proportion of input magnitude established by sCRACM (red). **C.** Excitatory synaptic input map to the three different dendritic domains of ttL5 pyramidal neurons. The height of ellipses represents dendritic location while width represents input strength. The tuft input map was generated from pia aligned maps while oblique and basal maps from soma (dashed line) aligned maps. Area names are ordered by relative peak location; asterisks mark FF areas. Only inputs > 0.6 pC are shown for clarity. NB: LP input magnitude is likely underestimated due to lower virus titer.

Taken together, these results show a remarkable specificity of synaptic targeting by brain-wide connections, with only a loose adherence to Peters' rule for the majority of inputs. This highlights that the location of many long-range inputs cannot be surmised on the basis of axonal branching and may not

follow clear rules associated with their position above or below the target area in a cortical hierarchy. Furthermore, the discrepancy between the numbers of rabies-labelled neurons and measured synaptic currents indicates that the former should be taken as a guide for anatomical connectivity and identity, but not the postsynaptic effects, of these inputs.

Discussion

Using an array of techniques for long-range circuit dissection, we have comprehensively mapped the location and dendritic targets of inputs to ttL5 neurons in the medial secondary visual cortex in mice. This allowed us to determine the dendritic targets of FF and FB connections and to make a direct assessment of Peters' rule for brain-wide connections.

The whole-brain input map generated via rabies tracing was qualitatively similar to previous results from the primary visual cortex (Kim et al 2015). Axonal projections from the rabies-identified input regions broadly followed the expected pattern, with FB projections being biased toward L1 and FF areas toward the deeper layers (D'Souza et al 2020, Harris et al 2019, Rockland & Pandya 1979). Accordingly, L1 was densely innervated by higher-order cortical areas like RSPg and ACA as well as the secondary thalamic nuclei (LP, ATN). Interestingly, ORB, a higher-order cortical region, displayed a projection pattern associated with FF areas. Additionally, the majority of ORB projection neurons were found in L2/3, another feature of FF connectivity. ORB is thus an exemption in terms of FB axonal projections.

In comparison to the strong similarities in axonal projections patterns, synaptic input maps showed a remarkable degree of heterogeneity. We used a novel approach to allocate sCRACM input to specific dendritic compartments by deconvolving the synaptic input maps with morphological ttL5 reconstructions, in which tuft, oblique, and basal compartments had been manually labelled. This revealed several unexpected results. The connection from VISp, which is a textbook example of FF connections and is thus generally assumed to primarily target perisomatic dendrites, was instead heavily biased towards the apical tuft. Conversely, the axons from ORB, which had a very similar, FF-like projection pattern, synapsed almost exclusively with basal and oblique dendrites. Furthermore, the location of synaptic input to individual neurons showed a strong correlation with soma depth, indicating that beyond the large overlap of axons and dendrites, ORB input targets each cell so as to preferentially form synapses at locations proximal to the soma. Other recorded areas (e.g. RSPg, ACA, ATN) showed some degree of conformity to Peters' rule, yet still with significant differences in the proportion of synapses generated in the different regions of high axonal projections. The only area where the correspondence was remarkable and Peter's rule held fully was LP.

Comparing anatomical connectivity obtained by rabies tracing to functional connectivity obtained by full-field optogenetic stimulation of axons revealed large and unexpected differences. However, several

348 technical caveats potentially biasing these results needs to be taken into account. First, the total input
349 proportion to a population of starter neurons does not necessarily represent faithfully the input proportions
350 received by single neurons, due to varying degrees of convergence from different input areas. We
351 attempted to minimize this effect by using a sparse Cre driver line to keep the number of starter cells low.
352 Second, the magnitude of optogenetically evoked input depends on the number of presynaptic cells
353 covered by viral injection. To mitigate this, we sought to cover a reasonably large fraction of each region
354 containing presynaptic cells by making several injections. Third, L5PNs can also be infected retrogradely
355 via their axonal projections to input areas, albeit with much lower probability. Recorded neurons with
356 direct photocurrent can be readily excluded based on the latency of sCRACM currents. However, likely
357 due to the dense reciprocal connectivity, LP injections resulted in a substantial number of retrogradely
358 labelled cells in V2m. This in turn could distort the LP synaptic input map by giving rise to unwanted local
359 input. To avoid this direct retrograde labelling, we injected a lower titer of virus into LP, which may have
360 caused an underestimation of LP input magnitude.

361 Despite these technical caveats, the detected discrepancy between anatomical and functional input
362 proportions estimated from the rabies tracing and sCRACM experiments is remarkable. There are several
363 possible explanations for this. First, there may be differing convergence of connectivity. For example,
364 inputs with strong rabies labelling but relatively weaker sCRACM input (like VISp and RSPg) may have
365 lower convergence, with a unique mapping of selected pre- and postsynaptic cells, perhaps carrying more
366 specific and detail-rich information to individual V2m neurons. Meanwhile, areas with strong synaptic
367 currents relative to their small rabies-labelled populations (like ORB and ACA) may have higher
368 convergence and be less discerning of their targets in order to convey more general contextual or state-
369 specific information. Second, there may be a difference in the strength of individual synapses not
370 reflected in rabies efficiency, with sparse input areas having disproportionately strong synapses.
371 However, the increase in the strengths of individual synapses required to overcome such a large
372 discrepancy seems rather unlikely. A third possible contributing factor could be the recently reported
373 activity-dependence of rabies transmission (Beier et al 2017). This would suggest that sparse input areas
374 (like ORB and ACA) have much lower activity despite their strong synaptic connections. Conversely, VISp
375 and RSPg should provide high activity input for the relatively modest synaptic input to results in extensive
376 rabies labelling.

377 Our results provide a complex picture regarding the possible interaction of FF and FB inputs (Figure 7C).
378 Functionally, V2m has been linked to visual motion processing (Sun et al 2009) and is thought to take
379 part in navigation and spatial processing as part of the dorsal stream (Glickfeld & Olsen 2017). Thalamic
380 FB input, which targets almost exclusively the apical tuft, arrives from multiple higher-order nuclei. Parts
381 of ATN receive strong vestibular input (Rancz et al 2015) and, together with RSP form a central part of
382 the head-direction system (Taube 2007, Velez-Fort et al 2018). It is thus likely that spatial and
383 multisensory contextual information carried by LP inputs (Roth et al 2016) interacts with FF visual input in
384 the tuft compartment. However, the role of tuft integration is likely to differ from primary sensory cortices,

385 considering that ttL5 neurons in the secondary visual cortex can have substantially different integrative
386 properties (Galloni et al 2020). Contrary to thalamic input, cortical FB inputs target all three dendritic
387 domains. Perhaps surprisingly, the strongest of these are ORB and ACA, which can interact with the local
388 FF input at the level of oblique and basal dendrites. Frontal cortices in general are involved in decision
389 making and executive control of behavior (Hamilton & Brigman 2015), and ORB in particular has been
390 shown to encode spatial goals (Feierstein et al 2006). ACA, meanwhile, can directly regulate visually
391 evoked responses and sensory discrimination in the primary visual cortex (Zhang et al 2014), and
392 contributes to learning to predict sensory input to primary visual cortex (Fiser et al 2016). Their precise
393 roles in the functioning of V2m, however, remains unknown.

394 A surprisingly large proportion (around half) of all the synaptic input, arrives at the oblique dendrites. This
395 is important as oblique dendrites are known to strongly affect L5 excitability (Schaefer et al 2003) and can
396 gate information flow from the apical dendrites (Jarsky et al 2005). While FB inputs targeting the apical
397 tuft have been suggested to act as a general gain control for ttL5 neurons, it is thus possible that ORB
398 and ACA perform a similar gating function, but perhaps with more specificity regarding input identity or
399 dendritic branches. Indeed, their particularly strong targeting of oblique dendrites might allow both fine-
400 level control of plasticity for FF synapses at these dendrites, while simultaneously allowing them to exert a
401 more binary gating control over input from both the thalamic nuclei and VISp, which all predominantly
402 arrive at the tuft. Furthermore, the large amount of cortical FB input to basal dendrites suggests a strong
403 amplification of local FF input close to the AP initiation zone.

404 In general, our results show that while the classification of areas as FF or FB can be based on axonal
405 projections (albeit with exceptions, such as ORB), macroscopic projectomes do not predict cell-type level
406 input location. We found that FF and FB inputs synapse on dendritic domains not purely determined by
407 projection and dendritic density, indicating that Peters' rule on the level of cell types is at best a weak
408 guideline. Similarly, while rabies tracing from a population of starter cells is an effective tool to study the
409 general wiring diagram, the proportion of input neurons thus estimated is likely to give a poor prediction of
410 functional input strength. Finally, the location and possible interactions between FF and the broad range
411 of FB inputs as well as their specific information content suggests that ttL5 neurons may be adopting a
412 multitude of integrative strategies that are different from those previously suggested.

413

Materials and Methods

Animals

All animal experiments were prospectively approved by the local ethics panel of the Francis Crick Institute (previously National Institute for Medical Research) and the UK Home Office under the Animals (Scientific Procedures) Act 1986 (PPL: 70/8935). All surgery was performed under isoflurane anesthesia, and every effort was made to minimize suffering. Transgenic mice were used: Tg(Colgalt2-Cre)NF107Gsat (RRID:MMRRC_036504-UCD, also known as Glt25d2-Cre) were crossed with the Ai14 reported line expressing tdTomato (RRID:IMSR_JAX:007908). Additionally, Tg(Rbp4-Cre)KL100Gsat/Mmucd (RRID:MMRRC_031125-UCD) mice were used to establish the efficacy of the cre-off approach. As only male mice are transgenic in the Colgalt2-Cre line, all experiments were done on male animals. Animals were housed in individually ventilated cages under a 12 hr light/dark cycle.

Viruses

EnvA-CVS-N2c$^{\Delta G}$-mCherry rabies virus, and adeno associated viruses expressing TVA and EGFP (AAV8-EF1a-flex-GT), N2c glycoprotein (AAV1-Syn-flex-H2B-N2CG), or Cre-OFF Chronos-GFP (AAV1-EF1-CreOff-Chronos-GFP) were a generous gift of Molly Strom and Troy Margrie. Chronos-GFP (also called ShChR) expressing adeno associated virus (rAAV1-Syn-Chronos-GFP) was obtained from UNC Vector Core.

Surgical procedures

Surgeries were performed on mice aged 3–8 weeks using aseptic technique under isoflurane (2–4%) anesthesia and analgesia (meloxicam 2 mg/kg and buprenorphine 0.1 mg/kg). The animals were head-fixed in a stereotaxic frame and a small hole (0.5–0.7 mm) was drilled in the skull above the injection site. Virus was loaded into a glass microinjection pipette (pulled to a tip diameter of around 20 µm) and pressure injected into the target region at a rate of 0.4 nl/s using a Nanoject III delivery system (Drummond Scientific). To reduce backflow, the pipette was left in the brain for approximately 5 min after completion of each injection.

For rabies virus tracing experiments, a 1:2 mixture of TVA and N2c glycoprotein expressing cre-dependent AAVs (10-20 nL) was injected at stereotaxic brain coordinates (ƛ - 0.8 mm, ML 1.6 mm, DV 0.6 mm). Rabies virus (50-100 nL) was injected 5-7 days later at the same site. Ten to twelve days later, animals were transcardially perfused under terminal anesthesia with cold phosphate-buffer (PB, 0.1 M) followed by 4% paraformaldehyde (PFA) in PB (0.1 M).

For the sCRACM experiments, Chronos-GFP expressing AAV was injected into one of the identified presynaptic regions. The virus was allowed to express for at least 3 weeks before acute brain slice

446 preparation. The range of stereotaxic coordinates for each region are listed in Figure 2--supplementary
447 table 1. The injected virus was Chronos-GFP for every region except V2m, where Cre-OFF Chronos-GFP
448 was instead used to avoid expression in the recorded Colgalt2-Cre neurons. For some of the injections in
449 LP, the Chronos-GFP virus was diluted by 10-fold in sterile cortex buffer before injection.

450 *Data acquisition and analysis for rabies tracing experiments*

451 Brain samples were embedded in 4-5% agarose (Sigma-Aldrich: 9012-36-6) in 0.1M PB and imaged
452 using serial two-photon tomography (Han et al 2018, Osten & Margrie 2013, Ragan et al 2012). Eight
453 optical sections were imaged every 5 µm with 1.2 µm x 1.2 µm lateral resolution, after which a 40µm
454 physical section was removed. Excitation was provided by a pulsed femto-second laser at 800 nm
455 wavelength (MaiTai eHP, Spectraphysics). Images were acquired through a 16X, 0.8 NA objective (Nikon
456 MRP07220) in three channels (green, red, blue) using photomultiplier tubes. Image tiles for each channel
457 and optical plane were stitched together with an open-source software written in MATLAB
458 (https://github.com/SainsburyWellcomeCentre/StitchIt). For cell detection, full resolution images were first
459 filtered with a Gaussian blur (sigma = 1) using Fiji (ImageJ 1.52e) to reduce imaging noise. The open-
460 source package cellfinder (DOI: 10.5281/zenodo.3891338; (Tyson et al 2020) was used for cell candidate
461 detection then classification. Automated mouse atlas propagation (Niedworok et al 2016) was used for
462 registration and segmentation on brain samples down-sampled to 10 µm voxels (to match the resolution
463 of the Allen CCFv3; (Wang et al 2020a). Cell coordinates were similarly down-sampled to 10 µm and the
464 number of cells was counted for each segmented area. For cell density visualisation, cell coordinates
465 were reverse-transformed onto the Allen CCFv3 space using the open source registration tool, Elastix
466 (Klein et al 2010) and were projected onto a 2D matrix in 10 µm / pixel resolution. For each unique cell
467 position, a cell density value was calculated as total cell counts in a nearby 9x9 pixel grid, normalized to
468 the sum of all starter or presynaptic cells. Data is reported as the percentage of all presynaptic cells
469 averaged across 3 experiments. Starter cell numbers were 7, 15, and 36.

470 *Acute slice preparation and electrophysiological recordings*

471 Adult mice were deeply anaesthetised with isoflurane and decapitated. The brain was rapidly removed
472 and placed in oxygenated ice-cold slicing solution containing (in mM): 125 sucrose, 62.5 NaCl, 2.5 KCl,
473 1.25 NaH_2PO_4, 26 $NaHCO_3$, 2 $MgCl_2$, 1 $CaCl_2$, 25 dextrose; osmolarity 340–350 mOsm. The cerebellum
474 and frontal cortex were removed manually with a coronal cut using a single-edged razor blade and the
475 rostral surface was affixed to a metal platform with cyanoacrylate glue. Coronal slices (300 µm thick)
476 between 2.6 and 3.5 mm posterior to bregma were prepared using a vibrating blade microtome (Leica
477 VT1200S). Slices were kept submerged in artificial cerebrospinal fluid (ACSF, containing in mM: 125
478 NaCl, 2.5 KCl, 1.25 NaH_2PO_4, 26 $NaHCO_3$, 1 $MgCl_2$, 2 $CaCl_2$, 25 dextrose; osmolarity 308–312 mOsm) at
479 35°C for the first 30–60 min after slicing, then at room temperature (22°C). All solutions and chambers
480 were continuously bubbled with carbogen (95% O2 / 5% CO2).

481 For recordings, individual slices were perfused in the recording chamber at a rate of approximately 6
482 mL/min with ACSF at room temperature (22°C), continuously bubbled with carbogen. To prevent axonal
483 spike propagation and enhance responses to optical stimulation, 1 µM tetrodotoxin (TTX) and 100 µM 4-
484 aminopyridin (4-AP) were added to the recording ACSF. This ensured that any light-evoked responses
485 were direct monosynaptic responses resulting from stimulation of Chronos-expressing axon terminals,
486 rather than from passing axons terminating in unknown locations on the dendrites.

487 Filamented borosilicate thick-walled glass micropipettes were pulled and heat-polished using a two-stage
488 horizontal puller (Zeitz DMZ Universal Electrode Puller) to obtain an electrode resistance of 3–6 MΩ. The
489 glass electrodes were filled with internal solution optimized for voltage clamp recordings, containing (in
490 mM): 120 $CsMeSO_3$ (CH_3O_3SCs), 3 CsCl, 10 HEPES, 1 EGTA, 4 Na_2ATP, 0.3 NaGTP, 5 Na_2-
491 phosphoreatine ($C_4H_8N_3O_5PNa_2$), 3.5 QX-314 chloride, 0.5 % (w/v) biocytin hydrochloride, 50 µM Alexa
492 Fluor 488 hydrazide; osmolarity 290–295 mOsm; pH adjusted to 7.3 with CsOH.

493 Visually guided whole-cell patch-clamp recordings from tdTomato-labelled Colgalt2-Cre neurons in V2m
494 were performed using a Scientifica SliceScope Pro 3000 microscope equipped with a 40x/0.8 NA
495 objective and an infrared (IR) Dodt Gradient Contrast system. The epifluorescence system used to
496 visualize fluorescent neurons was a CoolLED pE-4000 illumination system with a 550 nm peak excitation
497 wavelength. To avoid stimulating Chronos-expressing axons, epifluorescent illumination was kept to a
498 minimum during selection of cells to record. Recordings were made with a Multiclamp 700B amplifier
499 (Molecular Devices) in voltage-clamp configuration with a holding potential of -70 mV. Filtered signals
500 (8kHz low-pass) were digitized at 20 kHz with a National Instruments DAQ board (PCIe-6323). Acquisition
501 and stimulus protocols were generated in Igor Pro (Wavemetrics) with the NeuroMatic software package
502 (Rothman & Silver 2018). Throughout each recording, series resistance compensation was applied and
503 set to the highest value possible without inducing oscillations in the cell (typically between 40 and 75%).
504 Recordings wtih series resistance larger than 40 MΩ were excluded.

505 *Patterned optogenetic stimulation*

506 Optical stimulation was implemented using a digital micromirror device (DMD) with a 463 nm laser (laser-
507 coupled Polygon 400, Mightex Systems). The stimulus consisted of a 1000 x 500 µm grid divided into 24
508 x 12 spots of light (41.7 µm x 41.7 µm square) delivered through a 5x/0.15 NA dry objective (Olympus
509 MPlanFL N). The grid was approximately centered on the soma being recorded from, aligned to the pia
510 orthogonal to the apical dendrite. For each individual spot, the laser power was measured at the
511 specimen plane using a PM100D (Thorlabs) optical power meter equipped with a S121C sensor
512 (Thorlabs). The laser output associated with each spot was adjusted to obtain a measured power of
513 approximately 300 µW (173 mW/mm2).

514 Optical stimuli were delivered for 1 ms at 0.1 Hz in a pseudo-random sequence designed to maximise the
515 distance between consecutive spots and the time between stimulation of neighbouring spots. Each

516 recording trial consisted of a single repetition of all 288 stimuli followed by a full-field stimulus, in which all
517 stimulation spots were illuminated simultaneously for 1 ms. For each cell, 5-20 trials were recorded, with
518 30s pauses between trials, making the interval between consecutive stimulation of the same spot
519 approximately 60s. Following each recording, an image was taken to record the location of the recorded
520 cell (filled with Alexa Fluor 488) relative to the stimulation grid. This was used during analysis to align the
521 recorded sCRACM heatmap with the location of the pia or soma.

522 *Immunohistochemistry & morphological reconstructions*

523 After recording, slices were fixed overnight at 4°C in a 4% paraformaldehyde solution and were
524 subsequently kept in PBS. Slices were stained with DAPI (5 µg/mL) for 10 min, mounted on glass slides
525 and images were acquired with either a confocal microscope for high-resolution images (Leica SP5;
526 objective: 20x/0.7NA or 10x/0.4NA; pinhole size: 1 airy unit) or a slide scanner for visualizing injection
527 sites (Olympus VS120, objective: 4x/0.16NA). Image processing was done with the FIJI software package
528 (Schindelin et al 2012).

529 *Data analysis*

530 Analysis and data visualization were performed with custom macros and scripts written in Igor Pro and
531 MATLAB (Mathworks). Unless otherwise specified, all reported data values refer to the mean ± standard
532 error (SEM). Recordings were not corrected for liquid junction potential.

533 Recordings were baselined in a 40 ms window before each stimulus and averaged across trials, and the
534 peak and area of the evoked currents were measured in a 50 ms window after the stimulus. Stimulus
535 spots for which the peak current was lower than seven times the standard deviation of the baseline noise
536 were scored as zero.

537 For some of the injection sites, a degree of retrograde transport of the Chronos virus was noted in areas
538 outside of the primary injection site, including in V2m. A few recorded Colgalt2-Cre neurons in V2m were
539 thus found to be intrinsically expressing Chronos. This was easily detected in the recordings by an
540 instantaneous inward current at the onset of laser stimulation, in contrast to the 4-5 ms delay between
541 stimulus onset and sCRACM current observed normally. Any cells with no such delay were excluded from
542 the analysis.

543 Because peak response amplitudes varied between cells and preparations, to obtain average input
544 distributions from a presynaptic population, the heatmap for each cell was normalised to the peak EPSC
545 value for that cell. Heatmaps were then aligned horizontally by soma location and then vertically by either
546 soma or pia location before averaging each pixel across cells. For each cell, the soma could be localised
547 to within one quadrant of a given stimulation spot. When averaging across cells, the effective sampling
548 resolution (i.e. the pixel dimension) for the average sCRACM heatmaps and related horizontal and
549 vertical projections were thus approximately 20.8 µm (equal to half of the stimulus spot size, i.e. 1000/48

550 μm). All values reported for the locations of sCRACM inputs from different presynaptic regions are in
551 multiples of this number. Note, however, that the actual resolution with which synapses can be localised
552 in the heatmaps is likely to be lower than this, as it is limited by both light scattering in the tissue and by
553 the spread of voltage along stimulated axons, which is determined by the length constant of presynaptic
554 axons. Previous studies have indicated that these factors limit the actual sCRACM resolution to
555 approximately 60 μm (Petreanu et al 2009).

556 To estimate the proportion of sCRACM input targeting different dendritic domains, the recorded input map
557 for each cell was convolved with the average ttL5 morphology obtained from 11 reconstructed Colgalt2-
558 Cre neurons in V2m. This was done by manually separating the apical tuft, oblique (including the apical
559 trunk), and basal dendrites of the reconstructions in Neurolucida 360 and quantifying the total dendritic
560 length in 10 μm thick sections perpendicular to the main axis of the apical dendrite. The resulting dendrite
561 profiles were then aligned by the soma and averaged. Using this average morphology, at each distance
562 from the soma the proportion of dendrites belonging to each domain was calculated relative to the total
563 dendritic length within that section. For each sCRACM recording, these proportions were calculated using
564 an average morphology that was scaled to the soma-pia distance of the recorded cell. Each pixel of the
565 heatmap for that cell was then multiplied by these dendritic proportions to obtain the proportion of evoked
566 current assigned to each dendritic domain.

567 A similar calculation was performed to quantify the expected input profile on the basis of axon and
568 dendrite densities at each distance from the pia. In this case, the reconstructed morphologies were
569 aligned by the apical tuft before averaging. Both the axon and dendrite distributions were then normalised
570 to the peak of each curve and multiplied, resulting in large values at locations containing both axons and
571 dendrites.

572

573 # Acknowledgments

574 We thank Troy Margrie, Molly Strom, Thomas Mrsic-Flogel and Charlie Rousseau for help with data
575 acquisition and analysis of rabies tracing experiments. We are grateful to Florencia Iacaruso and Zoltán
576 Kisvárday for helpful comments on the manuscript.

577 **Competing interests:** The authors declare that no competing interests exist.

578

579

References

Aru J, Suzuki M, Larkum ME. 2020. Cellular Mechanisms of Conscious Processing. *Trends Cogn Sci* 24: 814-25

Beier KT, Kim CK, Hoerbelt P, Hung LW, Heifets BD, et al. 2017. Rabies screen reveals GPe control of cocaine-triggered plasticity. *Nature* 549: 345-50

Briggman KL, Helmstaedter M, Denk W. 2011. Wiring specificity in the direction-selectivity circuit of the retina. *Nature* 471: 183-8

Collins DP, Anastasiades PG, Marlin JJ, Carter AG. 2018. Reciprocal Circuits Linking the Prefrontal Cortex with Dorsal and Ventral Thalamic Nuclei. *Neuron* 98: 366-79 e4

D'Souza RD, Meier AM, Bista P, Wang Q, Burkhalter A. 2016. Recruitment of inhibition and excitation across mouse visual cortex depends on the hierarchy of interconnecting areas. *Elife* 5

D'Souza RD, Wang Q, Ji W, Meier AM, Kennedy H, et al. 2020. Canonical and noncanonical features of the mouse visual cortical hierarchy. *biorxiv.org*

Feierstein CE, Quirk MC, Uchida N, Sosulski DL, Mainen ZF. 2006. Representation of spatial goals in rat orbitofrontal cortex. *Neuron* 51: 495-507

Felleman DJ, Van Essen DC. 1991. Distributed hierarchical processing in the primate cerebral cortex. *Cereb Cortex* 1: 1-47

Fino E, Yuste R. 2011. Dense inhibitory connectivity in neocortex. *Neuron* 69: 1188-203

Fiser A, Mahringer D, Oyibo HK, Petersen AV, Leinweber M, Keller GB. 2016. Experience-dependent spatial expectations in mouse visual cortex. *Nat Neurosci* 19: 1658-64

Franklin KBJ, Paxinos G. 2007. *Paxinos and Franklin's The mouse brain in stereotaxic coordinates*. Amsterdam: Academic Press, an imprint of Elsevier. 1 volume (unpaged) pp.

Galloni AR, Laffere A, Rancz E. 2020. Apical length governs computational diversity of layer 5 pyramidal neurons. *Elife* 9

Glickfeld LL, Olsen SR. 2017. Higher-Order Areas of the Mouse Visual Cortex. *Annu Rev Vis Sci* 3: 251-73

Groh A, Meyer HS, Schmidt EF, Heintz N, Sakmann B, Krieger P. 2010. Cell-type specific properties of pyramidal neurons in neocortex underlying a layout that is modifiable depending on the cortical area. *Cereb Cortex* 20: 826-36

Guerguiev J, Lillicrap TP, Richards BA. 2017. Towards deep learning with segregated dendrites. *Elife* 6

Hamilton DA, Brigman JL. 2015. Behavioral flexibility in rats and mice: contributions of distinct frontocortical regions. *Genes Brain Behav* 14: 4-21

Han Y, Kebschull JM, Campbell RAA, Cowan D, Imhof F, et al. 2018. The logic of single-cell projections from visual cortex. *Nature* 556: 51-56

Harris JA, Mihalas S, Hirokawa KE, Whitesell JD, Choi H, et al. 2019. Hierarchical organization of cortical and thalamic connectivity. *Nature* 575: 195-202

Helmstaedter M, Briggman KL, Turaga SC, Jain V, Seung HS, Denk W. 2013. Connectomic reconstruction of the inner plexiform layer in the mouse retina. *Nature* 500: 168-74

Hooks BM, Mao T, Gutnisky DA, Yamawaki N, Svoboda K, Shepherd GM. 2013. Organization of cortical and thalamic input to pyramidal neurons in mouse motor cortex. *J Neurosci* 33: 748-60

Hubel DH, Wiesel TN. 1962. Receptive fields, binocular interaction and functional architecture in the cat's visual cortex. *J Physiol* 160: 106-54

Jarsky T, Roxin A, Kath WL, Spruston N. 2005. Conditional dendritic spike propagation following distal synaptic activation of hippocampal CA1 pyramidal neurons. *Nat Neurosci* 8: 1667-76

Kasthuri N, Hayworth KJ, Berger DR, Schalek RL, Conchello JA, et al. 2015. Saturated Reconstruction of a Volume of Neocortex. *Cell* 162: 648-61

Kim EJ, Juavinett AL, Kyubwa EM, Jacobs MW, Callaway EM. 2015. Three Types of Cortical Layer 5 Neurons That Differ in Brain-wide Connectivity and Function. *Neuron* 88: 1253-67

Kim JS, Greene MJ, Zlateski A, Lee K, Richardson M, et al. 2014. Space-time wiring specificity supports direction selectivity in the retina. *Nature* 509: 331-36

Klein S, Staring M, Murphy K, Viergever MA, Pluim JP. 2010. elastix: a toolbox for intensity-based medical image registration. *IEEE Trans Med Imaging* 29: 196-205

Krishnaswamy A, Yamagata M, Duan X, Hong YK, Sanes JR. 2015. Sidekick 2 directs formation of a retinal circuit that detects differential motion. *Nature* 524: 466-70

Larkum M. 2013. A cellular mechanism for cortical associations: an organizing principle for the cerebral cortex. *Trends Neurosci* 36: 141-51
Larkum ME, Petro LS, Sachdev RNS, Muckli L. 2018. A Perspective on Cortical Layering and Layer-Spanning Neuronal Elements. *Front Neuroanat* 12: 56
LeCun Y, Bengio Y, Hinton G. 2015. Deep learning. *Nature* 521: 436-44
Lee WC, Bonin V, Reed M, Graham BJ, Hood G, et al. 2016. Anatomy and function of an excitatory network in the visual cortex. *Nature* 532: 370-4
Little JP, Carter AG. 2012. Subcellular synaptic connectivity of layer 2 pyramidal neurons in the medial prefrontal cortex. *J Neurosci* 32: 12808-19
Niedworok CJ, Brown AP, Jorge Cardoso M, Osten P, Ourselin S, et al. 2016. aMAP is a validated pipeline for registration and segmentation of high-resolution mouse brain data. *Nat Commun* 7: 11879
Osten P, Margrie TW. 2013. Mapping brain circuitry with a light microscope. *Nat Methods* 10: 515-23
Packer AM, McConnell DJ, Fino E, Yuste R. 2013. Axo-dendritic overlap and laminar projection can explain interneuron connectivity to pyramidal cells. *Cereb Cortex* 23: 2790-802
Petreanu L, Mao T, Sternson SM, Svoboda K. 2009. The subcellular organization of neocortical excitatory connections. *Nature* 457: 1142-5
Ragan T, Kadiri LR, Venkataraju KU, Bahlmann K, Sutin J, et al. 2012. Serial two-photon tomography for automated ex vivo mouse brain imaging. *Nat Methods* 9: 255-8
Rancz EA, Moya J, Drawitsch F, Brichta AM, Canals S, Margrie TW. 2015. Widespread vestibular activation of the rodent cortex. *J Neurosci* 35: 5926-34
Reardon TR, Murray AJ, Turi GF, Wirblich C, Croce KR, et al. 2016. Rabies Virus CVS-N2c(DeltaG) Strain Enhances Retrograde Synaptic Transfer and Neuronal Viability. *Neuron* 89: 711-24
Rees CL, Moradi K, Ascoli GA. 2017. Weighing the Evidence in Peters' Rule: Does Neuronal Morphology Predict Connectivity? *Trends Neurosci* 40: 63-71
Richards BA, Lillicrap TP, Beaudoin P, Bengio Y, Bogacz R, et al. 2019. A deep learning framework for neuroscience. *Nat Neurosci* 22: 1761-70
Rieubland S, Roth A, Hausser M. 2014. Structured connectivity in cerebellar inhibitory networks. *Neuron* 81: 913-29
Rockland KS, Pandya DN. 1979. Laminar origins and terminations of cortical connections of the occipital lobe in the rhesus monkey. *Brain Res* 179: 3-20
Roth MM, Dahmen JC, Muir DR, Imhof F, Martini FJ, Hofer SB. 2016. Thalamic nuclei convey diverse contextual information to layer 1 of visual cortex. *Nat Neurosci* 19: 299-307
Rothman JS, Silver RA. 2018. NeuroMatic: An Integrated Open-Source Software Toolkit for Acquisition, Analysis and Simulation of Electrophysiological Data. *Front Neuroinform* 12: 14
Schaefer AT, Larkum ME, Sakmann B, Roth A. 2003. Coincidence Detection in Pyramidal Neurons Is Tuned by Their Dendritic Branching Pattern. *Journal of Neurophysiology* 89: 3143-54
Schindelin J, Arganda-Carreras I, Frise E, Kaynig V, Longair M, et al. 2012. Fiji: an open-source platform for biological-image analysis. *Nat Methods* 9: 676-82
Shipp S. 2016. Neural Elements for Predictive Coding. *Front Psychol* 7: 1792
Sun B, Lv B, Dong Q, Wang S, Chai Z. 2009. Watching moving images specifically promotes development of medial area of secondary visual cortex in rat. *Dev Neurobiol* 69: 558-67
Takahashi N, Ebner C, Sigl-Glockner J, Moberg S, Nierwetberg S, Larkum ME. 2020. Active dendritic currents gate descending cortical outputs in perception. *Nat Neurosci* 23: 1277-85
Takahashi N, Oertner TG, Hegemann P, Larkum ME. 2016. Active cortical dendrites modulate perception. *Science* 354: 1587-90
Taube JS. 2007. The head direction signal: origins and sensory-motor integration. *Annu Rev Neurosci* 30: 181-207
Tyson AL, Rousseau CV, Niedworok CJ, Keshavarzi S, Tsitoura C, Margrie TW. 2020.
Velez-Fort M, Bracey EF, Keshavarzi S, Rousseau CV, Cossell L, et al. 2018. A Circuit for Integration of Head- and Visual-Motion Signals in Layer 6 of Mouse Primary Visual Cortex. *Neuron* 98: 179-91 e6
Wang Q, Ding SL, Li Y, Royall J, Feng D, et al. 2020a. The Allen Mouse Brain Common Coordinate Framework: A 3D Reference Atlas. *Cell* 181: 936-53 e20
Wang XJ, Pereira U, Rosa MG, Kennedy H. 2020b. Brain connectomes come of age. *Curr Opin Neurobiol* 65: 152-61

690 Wickersham IR, Lyon DC, Barnard RJ, Mori T, Finke S, et al. 2007. Monosynaptic restriction of
691 transsynaptic tracing from single, genetically targeted neurons. *Neuron* 53: 639-47
692 Yamawaki N, Li X, Lambot L, Ren LY, Radulovic J, Shepherd GMG. 2019. Long-range inhibitory
693 intersection of a retrosplenial thalamocortical circuit by apical tuft-targeting CA1 neurons. *Nat*
694 *Neurosci* 22: 618-26
695 Zeng H. 2018. Mesoscale connectomics. *Curr Opin Neurobiol* 50: 154-62
696 Zhang S, Xu M, Kamigaki T, Hoang Do JP, Chang WC, et al. 2014. Selective attention. Long-range and
697 local circuits for top-down modulation of visual cortex processing. *Science* 345: 660-5

698

Supplementary material

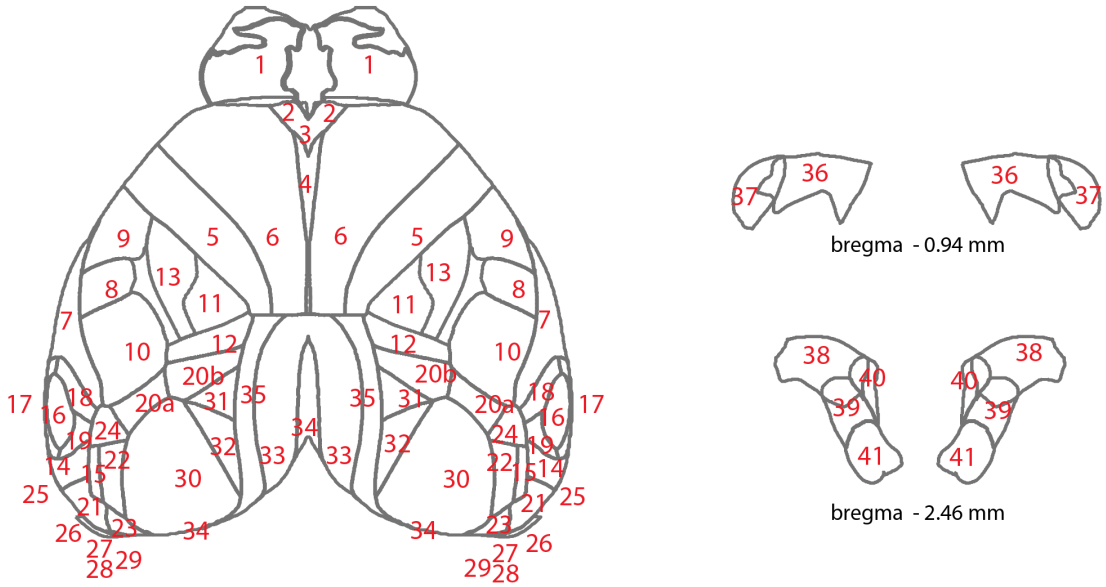

Cortex

1	Main olfactory bulb	MOB	20	Posterior parietal association areas	PTLp
2	Orbital area	ORB	20a	Rostrolateral visual area	VISrl
3	Prelimbic area	PL	20b	Anterior area	VISa
4	Anterior cingulate area	ACA	21	Postrhinal area	VISpor
5	Primary motor area	MOp	22	Lateral visual area	VISl
6	Secondary motor area	MOs	23	Posterolateral visual area	VISpl
7	Supplemental somatosensory area	SSs	24	Anterolateral visual area	VISal
8	Primary somatosensory area, nose	SSp-n	25	Ectorhinal area	ECT
9	Primary somatosensory area, mouth	SSp-m	26	Entorhinal area	ENT
10	Primary somatosensory area, barrel field	SSp-bfd	27	Presubiculum	PRE
11	Primary somatosensory area, lower limb	SSp-ll	28	Postsubiculum	POST
12	Primary somatosensory area, trunk	SSp-tr	29	Area prostriata	Apr
13	Primary somatosensory area, upper limb	SSp-ul	30	Primary visual area	VISp
14	Temporal association areas	TEa	31	Anteromedial visual area	VISam
15	Laterointermediate area	VISli	32	posteromedial visual area	VISpm
16	Primary auditory area	AUDp	33	Retrosplenial area, dorsal part	RSPd
17	Ventral auditory area	AUDv	34	Retrosplenial area, ventral part	RSPv
18	Dorsal auditory area	AUDd	35	Retrosplenial area, lateral agranular part	RSPagl
19	Posterior auditory area	AUDpo			

Thalamus

36	Lateral posterior nucleus of the thalamus	LP	39	Anteroventral nucleus of thalamus	AV
37	Dorsal part of the lateral geniculate complex	LGd	40	Anterodorsal nucleus	AD
38	Lateral dorsal nucleus of thalamus	LD	41	Anteromedial nucleus	AM

Figure 1—figure supplement 1. Brain parcellation and nomenclature according to CCFv3.

n = 3 experiments	average	SD	range
number of starter cells	19	15	7-36
total input cells	11622	2235	9059-13161
% contralateral input cells	6.30%	0.90%	

total input proportion (area / whole brain)								
thalamus	**average**	**sd**	**L1**	**L2/3**	**L4**	**L5**	**L6a**	**L6b**
LP	10.30%	1.70%						
LD	4.90%	0.80%						
AM	2.20%	0.50%						
LGd	1.70%	1.40%						
proximal cortex	**53.50%**							
VISp	10.60%	3.20%	1.83%	39.36%	8.10%	42.97%	5.97%	1.77%
VISpm	6.60%	1.80%	0.28%	16.63%	14.62%	55.98%	9.68%	2.80%
VISam	3.40%	1.50%	0.00%	15.12%	10.75%	60.37%	12.43%	1.32%
VISl	2.90%	1.50%	0.17%	25.97%	20.55%	46.06%	5.92%	1.33%
VISal	1.00%	0.80%	0.00%	20.08%	23.55%	50.62%	5.36%	0.40%
RSPv	14.70%	4.70%	0.29%	11.40%	n/a	70.43%	17.87%	0.01%
RSPd	8.50%	1.00%	0.29%	9.97%	n/a	65.15%	24.45%	0.14%
RSPagl	5.80%	1.70%	1.14%	24.25%	n/a	64.46%	9.96%	0.19%
distal cortex	**7.90%**							
ORB	2.70%	1.10%	19.25%	72.86%	n/a	6.22%	1.67%	0.00%
ACA	1.90%	1.00%	0.96%	12.20%	n/a	73.28%	13.56%	0.00%
PTLp (VISrl+VISa)	1.90%	1.00%	0.00%	11.16%	10.62%	65.23%	12.60%	0.39%
AUD	1.40%	0.50%	1.58%	17.60%	10.83%	60.17%	8.18%	1.64%

Figure 1—supplementary table 1. Results of presynaptic input tracing experiments. Areas highlighted in red are chosen for further study.

Area	Distance from bregma (mm)	Mediolateral distance (mm)	Depth from pia (mm)	Number & volume of injections
VISp	[−3.5 : −2.8]	[1.8 : 2.7]	[0.5 : 0.6]	3 x 100 nL
RSPg	[−3.2 : −2.7]	0.5	[0.5 : 0.7]	2 x 100 nL
V2m	[−3.2 : −2.7]	1	[0.2 : 0.5]	2 x 100 nL
ACA	[0 : 1]	0.5	[1.2 : 1.5]	3 x 100 nL
ORB	[2 : 2.8]	1	[1.5 : 2.3]	3 x 100 nL
ATN	[−0.5 : −1.2]	[0.5 : 0.7]	[3.2 : 3.3]	2 x 100 nL
LP	[−2.5 : −1.7]	[1 : 1.5]	[2.4 : 2.6]	3 x 100 nL

Figure 2—supplementary table 1. Stereotaxic coordinates and volumes of viral injections.

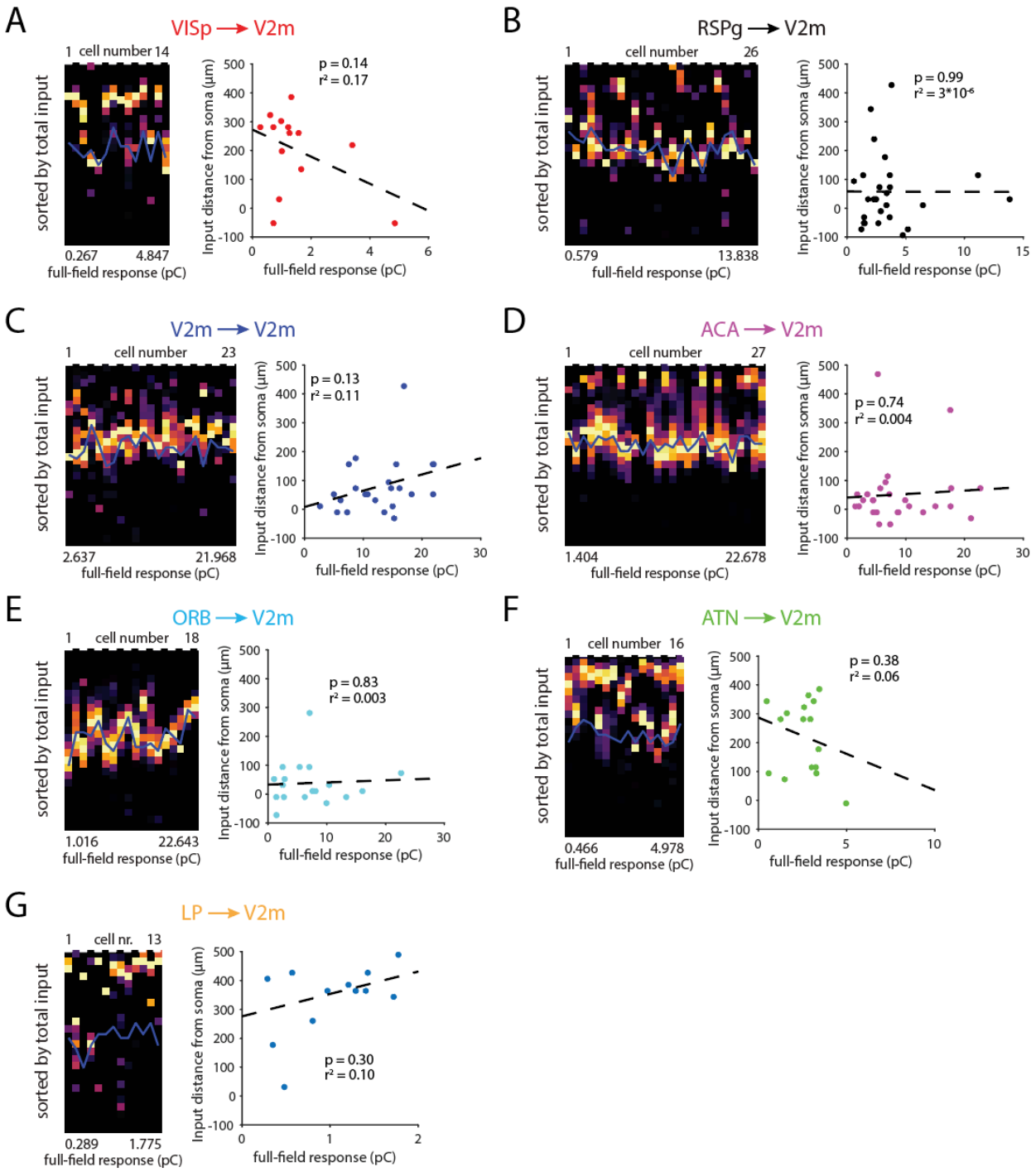

Figure 3—figure supplement 1. Input location does not correlate with input strength. A. Horizontal projections of VISp input to individual cells sorted by full-field stimulation response. Right: Location of the largest input peak versus full-field response. Dashed line is a linear fit. **B-G.** Same as in A, but for RSPg, V2m, ACA, ORB, ATN and LP input.

717

input area	parameter	basal	oblique	tuft*		
VISp	peak location (µm)	-63	21	198	total input (pC)	1.46
N = 7	input proportion (%)	18%	25%	57%	total input SEM	0.33
n = 14	proportional input (pC)	0.26	0.36	**0.84**	soma depth (µm)	493 ± 18
	horizontal bias (µm) **	41.7	41.7	20.8	cells with peak in tuft	10/14
V2m	peak location (µm)	-42	42	177	total input (pC)	12.61
N = 4	input proportion (%)	22%	61%	17%	total input SEM	1.17
n = 23	proportional input (pC)	**2.76**	**7.71**	**2.14**	soma depth (µm)	482 ± 12
	horizontal bias (µm) **	20.8	20.8	20.8	cells with peak in tuft	1/23
RSPg	peak location (µm)	-42	63	135	total input (pC)	3.56
N = 9	input proportion (%)	32%	42%	25%	total input SEM	0.58
n = 26	proportional input (pC)	**1.16**	**1.51**	**0.90**	soma depth (µm)	491 ± 13
	horizontal bias (µm) **	0	0	0	cells with peak in tuft	2/26
ACA	peak location (µm)	-42	21	94	total input (pC)	8.75
N = 5	input proportion (%)	30%	43%	27%	total input SEM	1.18
n = 27	proportional input (pC)	**2.64**	**3.77**	**2.34**	soma depth (µm)	461 ± 8
	horizontal bias (µm) **	0	20.8	-20.8	cells with peak in tuft	2/27
ORB	peak location (µm)	-42	21	N/A	total input (pC)	7.11
N = 3	input proportion (%)	37%	55%	8%	total input SEM	1.36
n = 18	proportional input (pC)	**2.63**	**3.94**	0.55	soma depth (µm)	502 ± 18
	horizontal bias (µm) **	0	0	0	cells with peak in tuft	0/18
ATN	peak location (µm)	-21	63	115	total input (pC)	2.55
N = 5	input proportion (%)	7%	25%	68%	total input SEM	0.30
n = 16	proportional input (pC)	0.17	**0.65**	**1.73**	soma depth (µm)	458 ± 11
	horizontal bias (µm) **	20.8	20.8	20.8	cells with peak in tuft	9/16
LP	peak location (µm)	-42	21	73	total input (pC)	0.97
N = 5	input proportion (%)	13%	18%	68%	total input SEM	0.15
n = 13	proportional input (pC)	0.13	0.18	**0.67**	soma depth (µm)	502 ± 19
	horizontal bias (µm) **	-41.7	62.5	-83.3	cells with peak in tuft	11/13
	total proportional input (pC)	**9.75**	**18.12**	**9.16**	**sum total input (pC)**	**37.03**

**tuft from pia, rest from soma*

*** negative means lateral, positive medial*

718

719 **Figure 4—supplementary table 1.** Results of all sCRACM experiments.

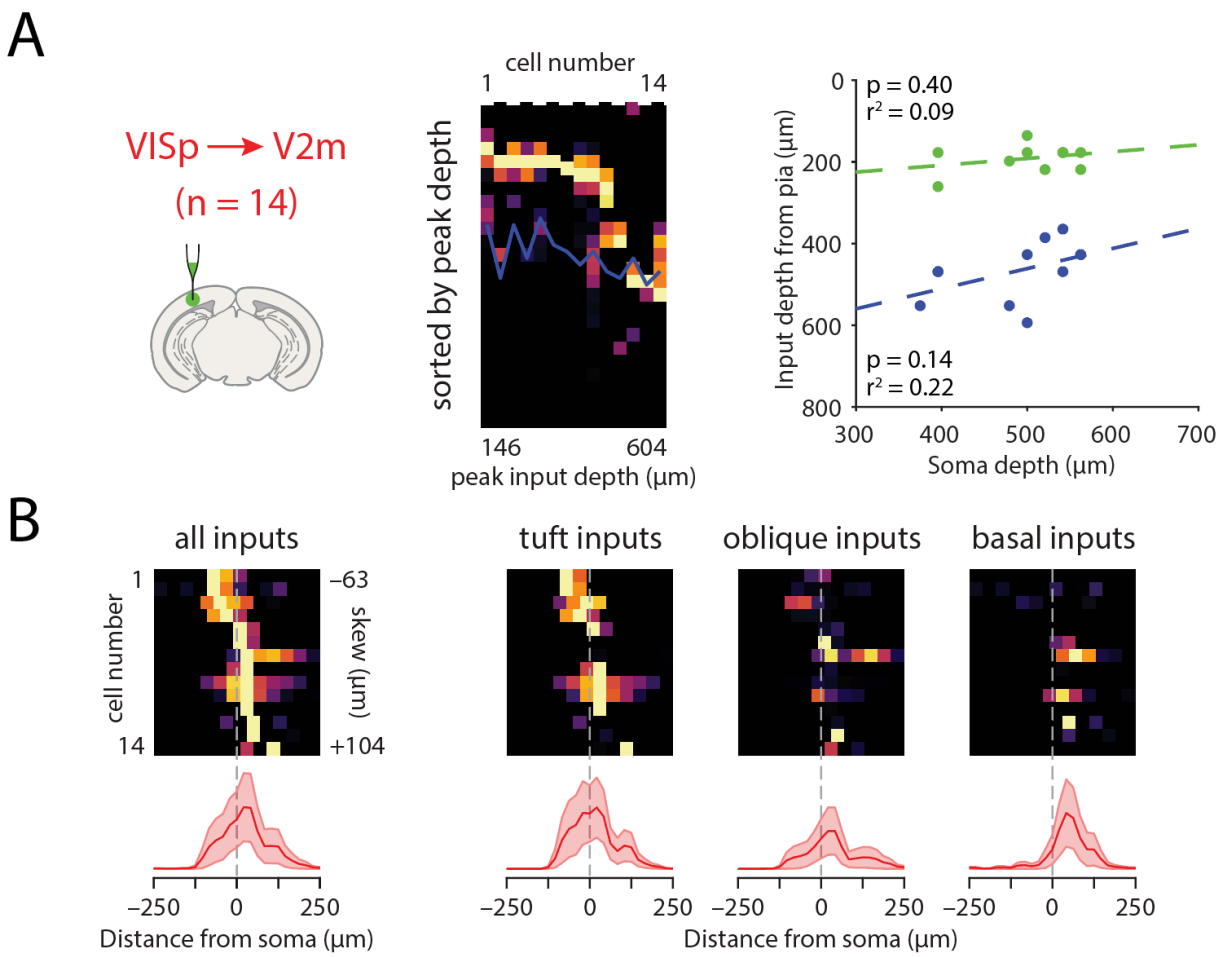

720

721 **Figure 4—figure supplement 1. Detailed data analysis for VISp. A.** Vertical projections of individual input maps
722 sorted by the location of the peak input. Right: Distance of tuft (green, defined as above the apical trough in the
723 vertical projection) and perisomatic (blue, defined as below the apical trough in the vertical projection) input peaks
724 from pia versus soma depth. Dashed lines are linear fits. **B.** Horizontal projections of individual input maps and their
725 average for all, and for domain-separated inputs.

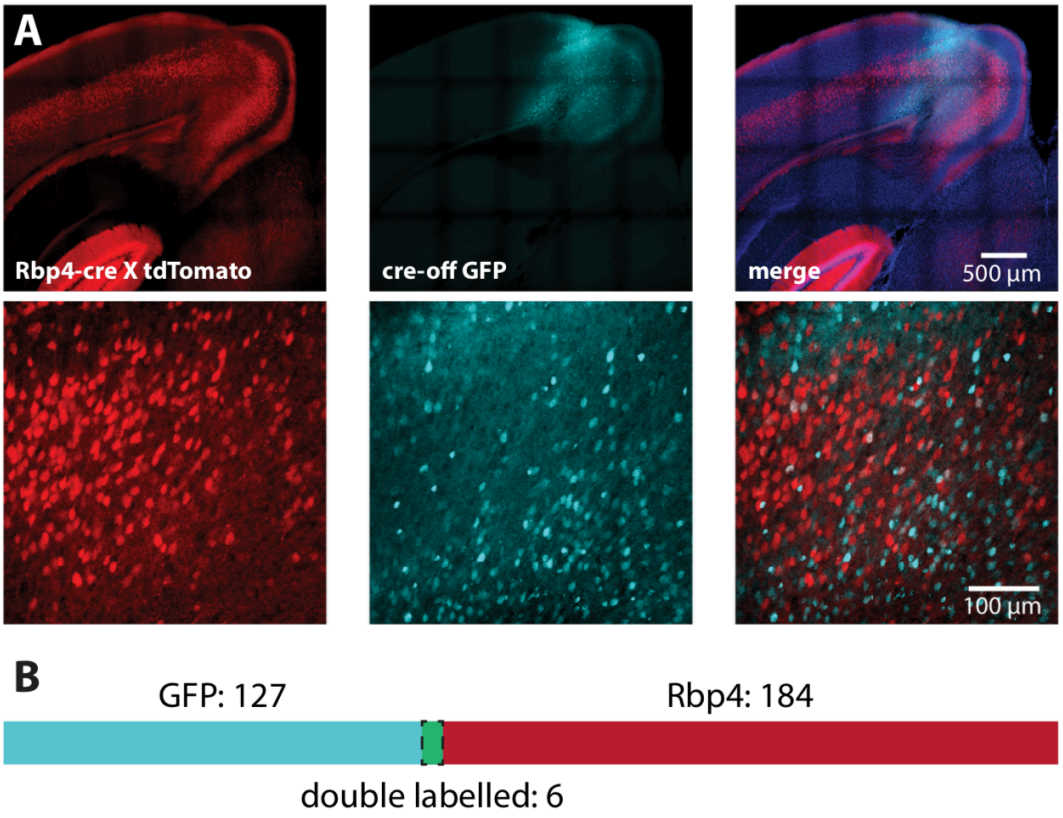

Figure 4—figure supplement 2. Efficacy of Cre-off virus. A. Example confocal images showing cre expression in L5 pyramidal neurons (red), GFP expression following cre-off virus injection (cyan) and overlap (blue = DAPI) on two magnifications. **B.** Quantification of overlap between cre and GFP expression.

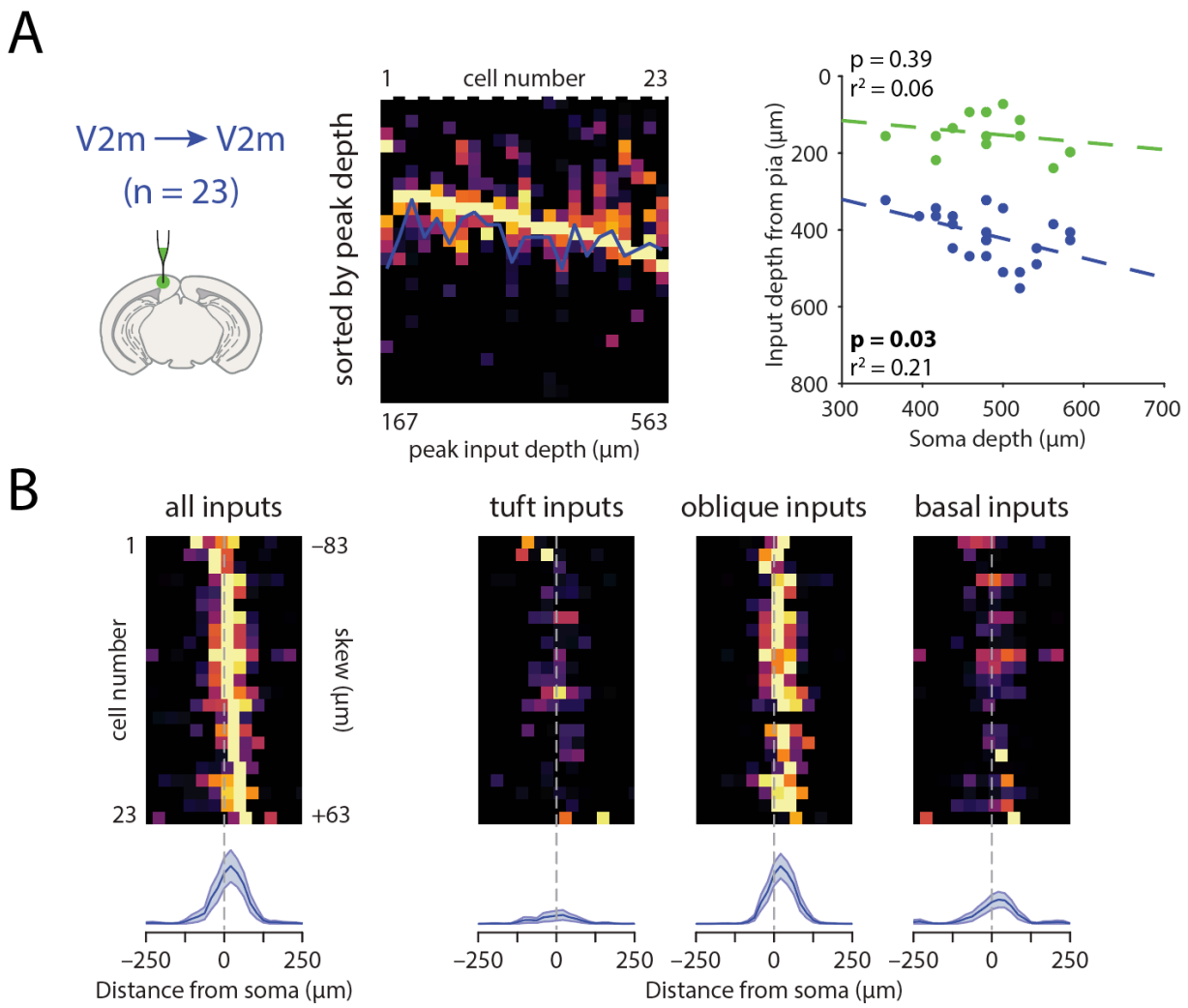

Figure 4—figure supplement 3. Detailed data analysis for V2m. A. Vertical projections of individual input maps sorted by the location of the strongest input. *Right:* Distance of tuft (green) and perisomatic (blue) input peaks from pia versus soma depth. Dashed lines are linear fits. **B.** Horizontal projections of individual input maps and their average for all, and for domain-separated inputs.

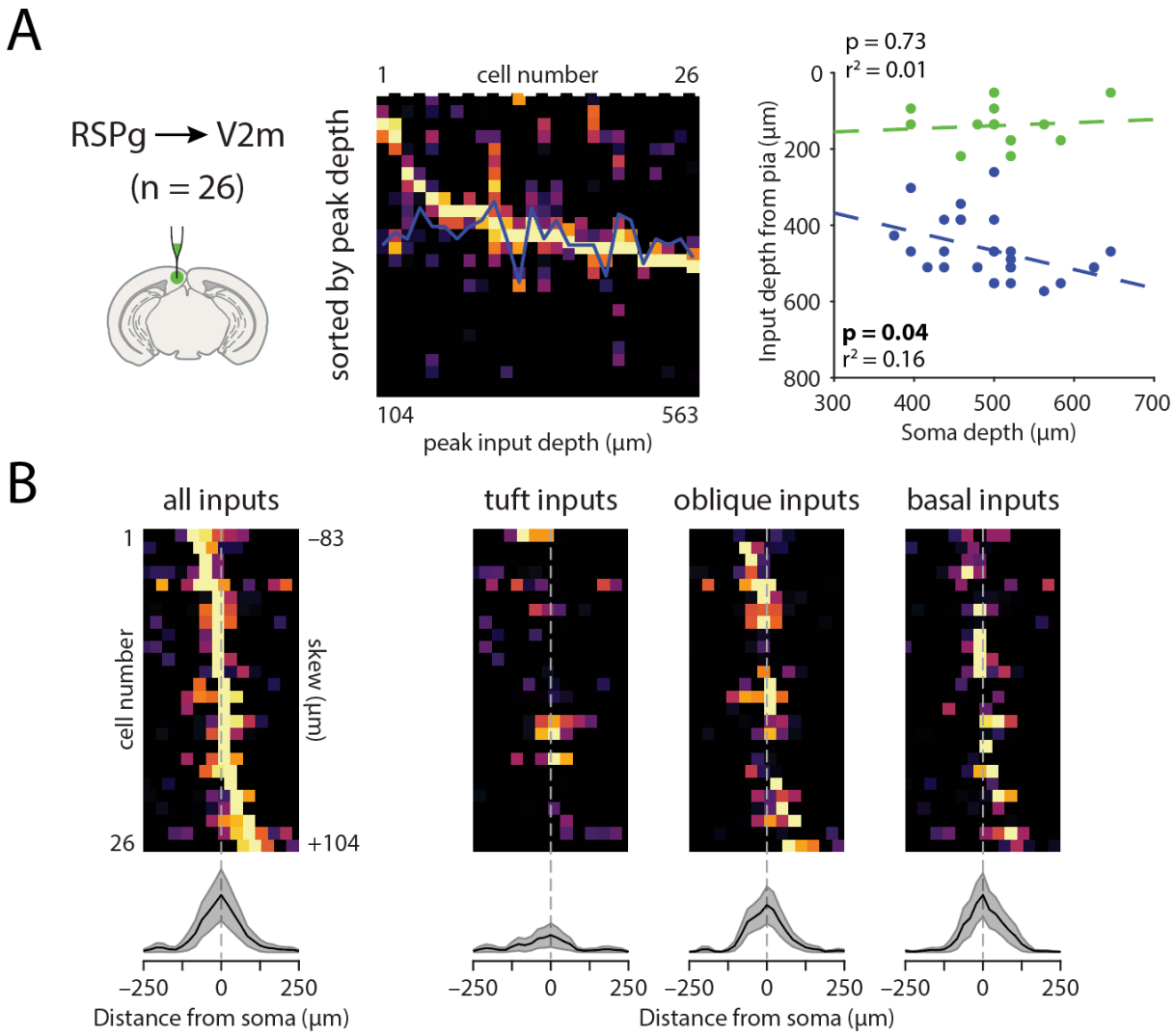

Figure 5—figure supplement 1. Detailed data analysis for RSPg. A. Vertical projections of individual input maps sorted by the location of the strongest input. *Right:* Distance of tuft (green) and perisomatic (blue) input peaks from pia versus soma depth. Dashed lines are linear fits. **B.** Horizontal projections of individual input maps and their average for all, and for domain-separated inputs.

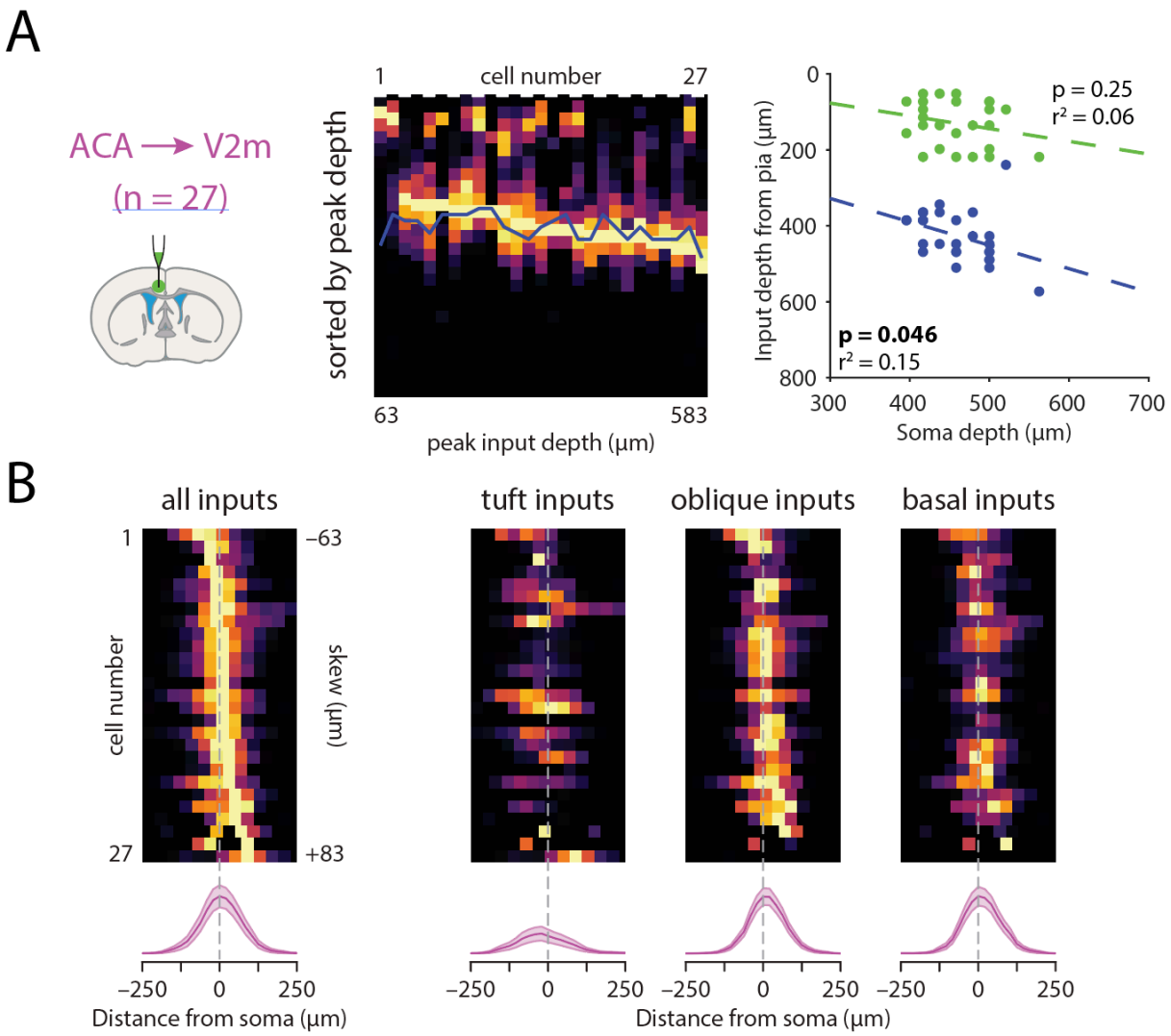

Figure 5—figure supplement 2. Detailed data analysis for ACA. A. Vertical projections of individual input maps sorted by the location of the strongest input. *Right:* Distance of tuft (green) and perisomatic (blue) input peaks from pia versus soma depth. Dashed lines are linear fits. **B.** Horizontal projections of individual input maps and their average for all, and for domain-separated inputs.

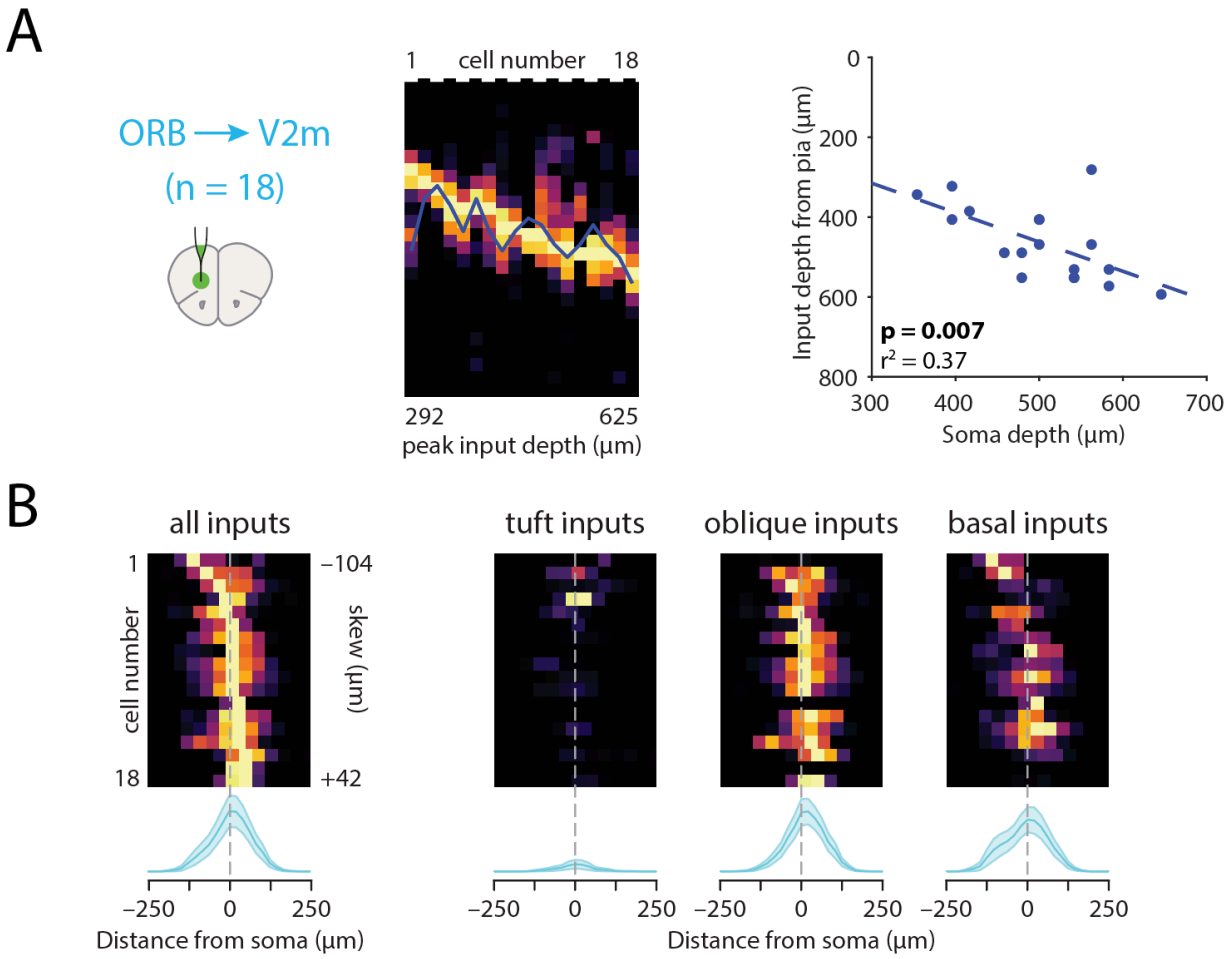

745

746 **Figure 5—figure supplement 3. Detailed data analysis for ORB. A.** Vertical projections of individual input maps
747 sorted by the location of the strongest input. *Right:* Distance of the perisomatic input peak from pia versus soma
748 depth. Dashed line is linear fit. **B.** Horizontal projections of individual input maps and their average for all, and for
749 domain-separated inputs.

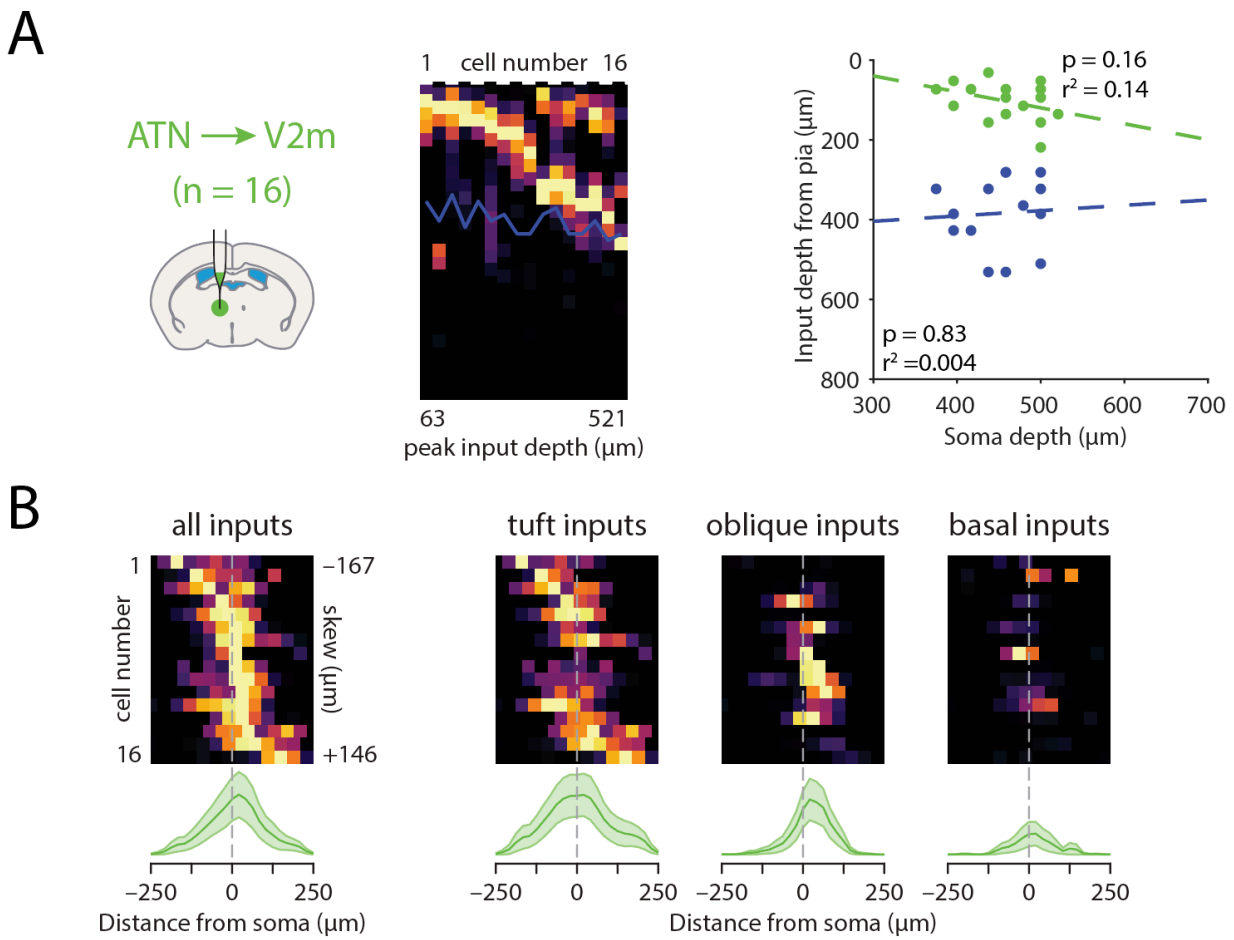

Figure 6—figure supplement 1. Detailed data analysis for ATN. A. Vertical projections of individual input maps sorted by the location of the strongest input. *Right:* Distance of tuft (green) and perisomatic (blue) input peaks from pia versus soma depth. Dashed lines are linear fits. **B.** Horizontal projections of individual input maps and their average for all, and for domain-separated inputs.

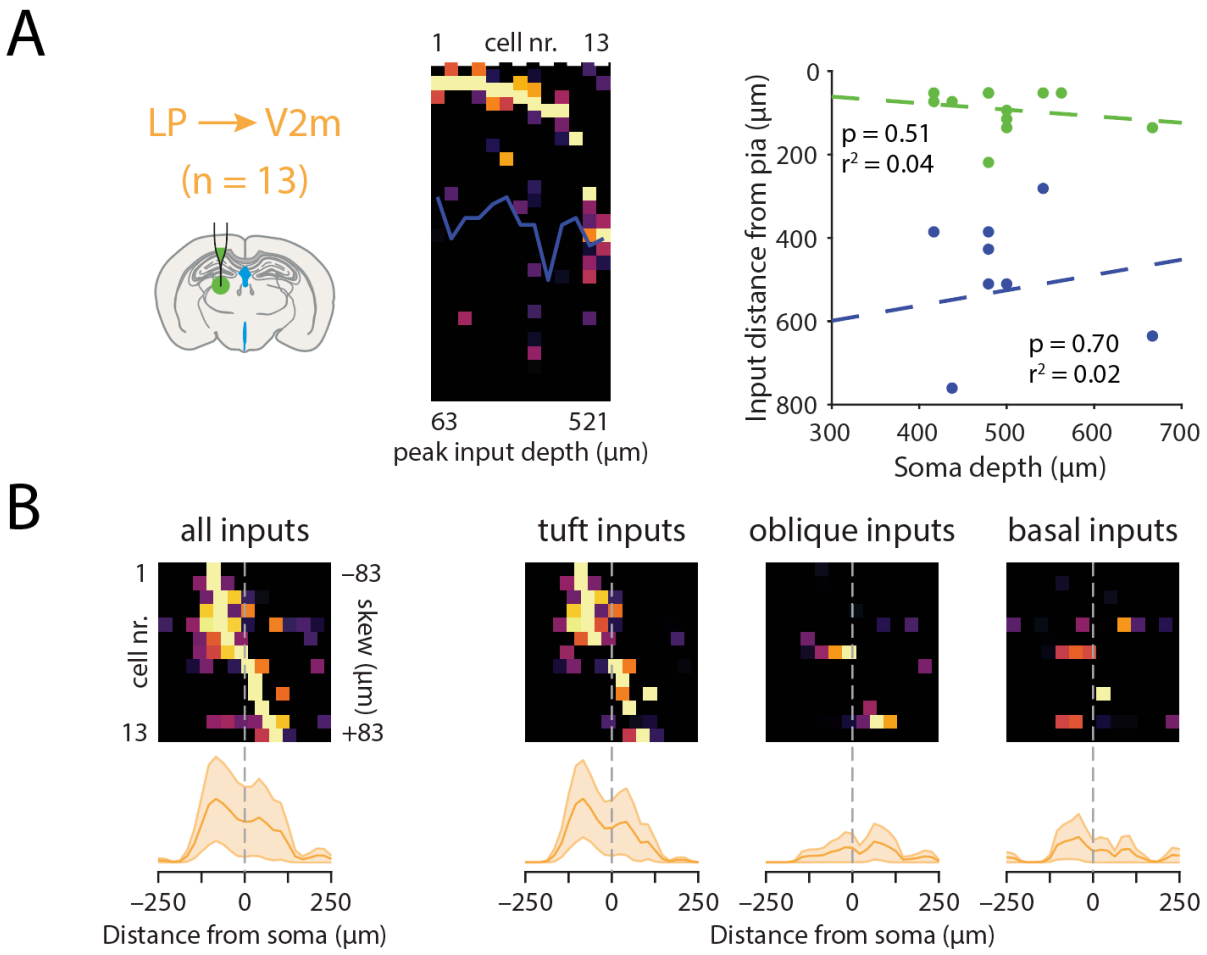

Figure 6—figure supplement 2. Detailed data analysis for LP. A. Vertical projections of individual input maps sorted by the location of the strongest input. *Right:* Distance of tuft (green) and perisomatic (blue) input peaks from pia versus soma depth. Dashed lines are linear fits. **B.** Horizontal projections of individual input maps and their average for all, and for domain-separated inputs.